HELSINKI UNIVERSITY OF TECHNOLOGY
Department of Electrical and Communications Engineering
Radio Laboratory

Aki Karttunen

Design of a 650 GHz dual reflector feed system

The thesis was submitted in partial fulfilment for the degree of Master of Science in Espoo, May 8, 2006.

Supervisor

Professor Antti Räisänen

Instructor

Mr. Janne Häkli, Lic.Sc.(Tech)

Author: Aki Karttunen

Name of the Thesis: Design of a 650 GHz dual reflector feed system

Date: May 8, 2006 **Number of pages:** 70

Department: Department of Electrical and Communications Engineering

Professorship: Radio Engineering

Supervisor: Professor Antti Räisänen

Instructor: Mr. Janne Häkli, Lic.Sc.(Tech)

A hologram can be used as a collimating element in a compact antenna test range (CATR) at millimetre and sub-millimetre wavelengths. The performance of a hologram can be improved by modifying the illumination of the hologram with a dual reflector feed system (DRFS). A 650 GHz dual reflector feed system (DRFS) was designed as part of an ESA project aiming at the measurement of a 1.5 m antenna at 650 GHz during autumn 2006. Design of the 650 GHz DRFS is presented and simulation results are presented and compared to the desired hologram illumination.

Hologram designed for the modified illumination is used only to transform the spherical wave illuminating the hologram to the planar wave in the quiet-zone (QZ). The -1 dB beam width of the illumination defines directly the -1 dB beam width of the QZ, i.e., the DRFS beam defines the QZ size. The desired illumination has flat amplitude in the middle, corresponding to a 2 m QZ diameter and -10 dB amplitude tapering on the hologram edge. Using the DRFS, the variation in slot widths in the hologram pattern is smaller compared to the previously used Gaussian illumination, which should improve the polarization performance of the hologram.

The reflector surfaces were synthesized with a geometrical optics (GO) based synthesis method and optimized based on the simulations with physical optics (PO) and physical theory of diffraction (PTD). A DRFS has been previously designed with the same synthesis method for 310 GHz. The designed 650 GHz DRFS has, despite the higher frequency, wider beam and significantly better beam quality. The simulations of the designed 650 GHz DRFS show excellent results. The -1 dB beam width diameter is about 2.34 m, which corresponds to a 1.96 m QZ diameter, and the hologram edge illumination is less than -10 dB. The maximum amplitude ripple in the -1 dB beam area is 0.45 dB peak-to-peak (0.24 dB rms) and the phase deviation is 5° peak-to-peak (0.8° rms).

Keywords: sub-millimetre wavelengths, shaped reflector antenna, feed system, reflector synthesis, geometrical optics (GO), ray tracing

Teknillinen Korkeakoulu **Diplomityön tiivistelmä**

Tekijä: Aki Karttunen

Työn nimi: Kaksiheijastimisen syötön suunnittelu 650 GHz:n taajuudelle

Päivämäärä: 08.05.2006 **Sivumäärä:** 70

Osasto: Sähkö- ja tietoliikennetekniikan osasto

Professuuri: Radiotekniikka

Työn valvoja: Professori Antti Räisänen

Työn ohjaaja: TkL Janne Häkli

Hologrammia voidaan käyttää suuntaavana elementtinä kompaktissa antennimittauspaikassa millimetri- ja alimillimetriaaltoalueilla. Hologrammin toimintaa voidaan parantaa muotoilemalla hologrammin valaisua kaksiheijastimisella syöttöjärjestelmällä. Tässä diplomityössä on suunniteltu kaksiheijastiminen syöttö 650 GHz:n taajuudelle osana ESA:n projektia, joka tähtää 1.5 m:n antennin mittaamiseen syksyn 2006 aikana. Tässä työssä kuvataan kyseisen syöttöjärjestelmän suunnittelu ja esitellään simulointitulokset.

Muotoillulle valaisulle suunniteltu hologrammi muuntaa hologrammille tulevan palloaalton tasoaaltoksi mitattavan antennin alueelle, eli ns. hiljaisele alueelle. Muotoillun valaisun -1 dB:n keilaleveys määrää suoraan hiljaisen alueen koon. Halutulla muotoillulla valaisulla on tasainen amplitudi keilan keskellä, jonka halkaisija vastaa 2 m halkaisijaltaan olevaa hiljaista aluetta, ja -10 dB:n amplituditaperointi hologrammin reunoilla. Käytettäessä muotoiltua valaisua raon leveyksien vaihtelu on peinempää hologrammin kuviossa verrattuna aiemmin käytettyyn gaussiseen valaisuun, minkä pitäisi parantaa hologrammin polarisaatio-ominaisuuksia.

Heijastinpinnat laskettiin geometriseen optiikkaan (GO) perustuvalla synteesimenetelmällä ja optimoitiin simuloineilla, joissa käytettiin fysikaalista optiikkaa (PO) ja fysikaalista diffraktioteoriaa (PTD). Kaksiheijastiminen syöttöjärjestelmä on aiemmin suunniteltu 310 GHz:n taajuudelle käyttäen samaa heijastimien synteesimenetelmää. Huolimatta suuremmasta taajuudesta suunnitellulla 650 GHz:n syöttöjärjestelmällä on suurempi keilanleveys ja merkittävästi parempi keilan laatu. Simulointitulokset ovat erittäin lupaavia: -1 dB:n kailanleveys vastaa 1.96 m:n hiljaista aluetta ja amplituditaperointi hologrammin reunalla on alle -10 dB. -1 dB:n keilan alueella amplitudivaihtelu on alle 0.45 dB huipusta huippuun (0.24 dB rms) ja vaiheen poikkeama palloaallosta on alle 5° huipusta huippuun (0.8° rms).

Avainsanat: alimillimetriaallot, muotoiltu heijastinantenni, syöttöjärjestelmä, heijastinantennisynteesi, geometrinen optiikka, säteenseuranta

Preface

This work has been done in MilliLab, Radio Laboratory of Helsinki University of Technology, and partially funded by the Academy of Finland trough its Centre-of-Excellence program SMARAD. This work has been done as a part of project supported by ESA, ESTEC Contract No. 19131/05/NL/LvH. VTT and Ticra are acknowledged for allowing the author to use their GRASP8W software for the simulations.

I would like to thank my instructor Janne Häkli and my supervisor professor Antti Räisänen for their help in preparing this thesis.

Espoo, May 8, 2006

Aki Karttunen

Table of contents

List of symbols

a	Horizontal half-axis of an ellipse
A	Area
b	Vertical half-axis of an ellipse
D	Output field aperture diameter, diameter of an antenna
D_{holo}	Diameter of the hologram
e	Eccentricity
E	Electric field amplitude
E_{ave}	Average electric field
E_{far}	Electric field in the far field
$\overline{E}$, $\overline{E}_0$	Electric field
$\overline{E}_{PO}$	Electric field computed with physical optics
$\overline{E}_{PTD}$	Electric field computed with physical theory of diffraction
f	Focal length
f_{holo}	Focal length of the hologram
f_{sub}	Focal length of the subreflector
F	Field accuracy
F_{holo}	Focal point of the hologram
h	Height
$\overline{H}$, $\overline{H}_0$	Magnetic intensity
$\overline{H}_i$	Incident magnetic intensity
i	Index, imaginary unit
j	Imaginary unit
$\overline{J}_e$	Electric surface current density
$\overline{k}$	Local wave vector
k, k_0	Wave number
l	Ray length
L	Eikonal function
M	Index
n	Index of refraction, index
$\overline{n}$	Surface normal vector
N	Index, degree of a function
P	Power

r	Distance
$r,\ \phi,\ \theta$	Spherical coordinates
$\bar{r}$	Vector
r_{main}	Main reflector distance
r_{sub}	Subreflector distance
R_1, R_2	Radius of curvature
$s,\ s_0$	Distance
$\bar{s}_i,\ \bar{s}_r$	Directional vector
S	Surface
$\bar{S}_0$	Poynting vector
$\bar{t},\ \bar{t}_0$	Tangential vector
x, y, z	Cartesian coordinates
X	Field error
Y	Field difference

α_{feed}	Feed horn direction angle
α_{sub}	Subreflector direction angle
β_{feed}	Angle of the feed horn coordinates
β_{main}	Angle of the main reflector coordinates
β_{sub}	Angle of the subreflector coordinates
ε	Surface error
ε_0	Permittivity of free space
ε_r	Relative permittivity
η	Aperture efficiency
η_0	Wave impedance of free space
θ_{feed}	Feed horn half-beam width
θ_{main}	Main reflector half-beam width
$\bar{\kappa}_1,\ \bar{\kappa}_2$	Direction of curvature
λ	Wavelength
μ_0	Permeability of free space
μ_r	Relative permeability
$\rho,\ \phi,\ z$	Polar coordinates
ω	Angular frequency

List of abbreviations

AUT	Antenna Under Test
CATR	Compact Antenna Test Range
DRFS	Dual Reflector Feed System
ESA	European Space Agency
FDTD	Finite-Difference Time-Domain
GO	Geometrical Optics
NURBS	Non-Uniform Rational B-Splines
PO	Physical Optics
PTD	Physical Theory of Diffraction
QPS	Quintic Pseudospline
QZ	Quiet-Zone
RAM	Radar Absorbing Material
RFQM	Radio Frequency Qualification Model
RCS	Radar Cross Section
RTO	Representative Test Object
TKK	Helsinki University of Technology

1 Introduction

Large millimetre and sub-millimetre wave antennas are commonly used in radio astronomy. Several ongoing space research projects will study the Universe at sub-millimetre wavelengths. Electrically large reflector antennas are needed for high angular resolution. For example European Space Agency (ESA) has a plan to launch the Planck satellite in 2008. The Planck satellite will be used to study the temperature anisotropies of cosmic microwave background at the frequencies from 30 GHz to 900 GHz. The satellite has a Gregorian telescope with a 1.5 metre main reflector.

Figure 1.1 Planck satellite [ESA].

The satellite antennas need to be tested before the launch to ensure their proper functioning. The measurements of large sub-millimetre wave antennas are very challenging. Because of the long far-field distance and the large atmospheric attenuation only choices are near-field measurements and compact antenna test ranges (CATRs). MilliLab/Radio Laboratory at the Helsinki University of Technology (TKK) has developed a hologram-based compact antenna test range. In a hologram-based antenna test range, the hologram is used to transform a spherical wave to a plane wave. The hologram is the binarized interference pattern of these two wave fronts which generates one when illuminated with the other. A hologram-based antenna test range have been

used to measure large sub-millimetre wave reflector antennas at frequencies up to 322 GHz [Lönnqvist 2005], [Häkli 2005b].

Manufacturing of large holograms with high pattern accuracy has been challenging. Traditionally a corrugated feed horn has been used to illuminate the hologram. Because of the high edge illumination, narrow slots have been needed at the edges of the hologram. These narrow slots are difficult to manufacture accurately and limit the use of the hologram to the polarization parallel to the slots, i.e., the vertical polarization. The narrow slots can be avoided with the use of a dual reflector feed system (DRFS). In the DRFS two shaped reflectors are used to modify the amplitude and phase of the field radiated by the corrugated feed horn. With DRFS it is possible to realize the amplitude tapering in the illumination of the hologram. Previously, a 310 GHz DRFS for hologram-based CATR has been demonstrated at 310 GHz [Häkli 2005c].

The design of a 650 GHz DRFS is presented in this paper. The reflector surfaces were synthesized with a geometrical optics (GO) based synthesis method and optimized based on the simulations with physical optics (PO) and physical theory of diffraction (PTD). The same synthesis method was used as for the 310 GHz DRFS. The designed 650 GHz DRFS has, despite the higher frequency, wider beam and significantly better beam quality.

In Chapter 2 the antenna measurement techniques are presented. Basic reflector antenna geometries are presented in Chapter 3 and reflector antenna radiation analysis methods used in the design of the DRFS are described. Reflector synthesis methods are presented in Chapter 4. In Chapter 5 the design of the 650 GHz DRFS is presented and simulation results in Chapter 6. Discussion on the synthesis and design methods and future work in Chapter 7 and conclusions are in Chapter 8.

2 Antenna measurement techniques

Antenna measurement techniques can be divided into three basic types: far-field measurements, near-field scanning techniques and compact antenna test ranges. At low frequencies it is possible to place the measured antenna in the far-field. The far-field criterion is

$$r = \frac{2D^2}{\lambda}, \tag{2.1}$$

where D is the diameter of the antenna and λ is the wavelength. The far field criterion is defined as the distance from the antenna where the distance to the edge of the antenna is $\lambda/16$ longer than the distance to the centre of the antenna, i.e., phase deviation from a plane wave is 22.5°. Usually a distance up to 20-50 times the far-field criterion is needed for accurate measurements. At millimetre and sub-millimetre wavelengths the far-field criterion can be tens of kilometres and atmospheric attenuation is very high; therefore far-field measurements are not possible.

In near-field scanning techniques the antenna radiation is measured in the near field and the far-field radiation is calculated from the near-field data for example using the Fourier-transform. The near-field is measured by taking samples of the field. The samples can be taken for example on a plane, a sphere or a cylinder surface [Lehto 2001]. In planar near-field scanners the sampling interval has to be smaller than $\lambda/2$ for the full angular coverage and position accuracy better than $\lambda/100$. The measurements of large high frequency antennas is very challenging because of the required high dynamic range, probe position accuracy and high number of sampling points. Near-field measurements have been used at frequencies up to 500 GHz [Lehto 2001].

In a compact antenna test range (CATR) the plane wave is generated, i.e., effectively far-field conditions, by a collimating element. CATRs are described in Sections 2.1 and 2.2.

2.1 Compact antenna test ranges

A compact antenna test range (CATR) can be used to measure the radiation pattern of an antenna. At millimetre and sub-millimetre wavelengths the far field distance is too long

and the atmospheric attenuation too high for antenna measurements. In a CATR, a reflector, two or three reflectors, a lens or a hologram is used as a collimating element to transform a spherical wave-front to a plane wave [Lehto 2001]. The plane wave region is called the quiet-zone (QZ) of the CATR and the antenna under test (AUT) is placed in the quiet-zone. Usually ripple of 1 dB peak-to-peak and 10° peak-to-peak is allowed at maximum in the quiet-zone field amplitude and phase, respectively.

The most common CATR is based on a reflector or a set of reflectors. Reflector based compact antenna test ranges are used at frequencies up to 200 GHz [Habersack 1991]. The main reflector has to be larger than the quiet-zone and the quiet-zone diameter is typically about 1/3 of the main reflector diameter for a single reflector CATR and 2/3 for dual reflector CATR [Lehto 2001]. Reflector geometries used are a single offset reflector, a dual cylindrical reflector, a dual offset reflector and a triple offset reflector. Examples of CATR geometries are illustrated in Figure 2.1.

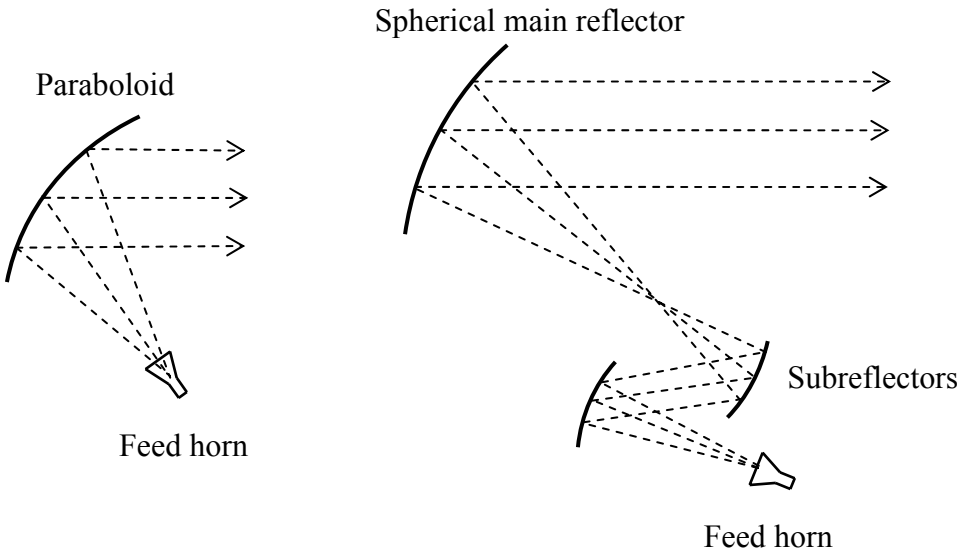

Figure 2.1 A single offset reflector and a trireflector CATR.

In general, the surface accuracy of the CATR reflectors has to be better than that of the antenna under test. Very large and accurate reflectors are very expensive and difficult to manufacture. Usually the surface accuracy limits the highest measurement frequency. Generally the accuracy requirement is about $\lambda/100$.

2.2 Hologram-based compact antenna ranges

A hologram can be used as a collimating element in a compact antenna test range [Hirvonen 1997]. The hologram is a binarized interference pattern of the wave-front illuminating the hologram and the desired plane wave in the quiet-zone. A schematic layout of a hologram-based CATR is shown in Figure 2.2. An offset angle of 33° is used to avoid unwanted diffraction orders and to reduce the ripples in the quiet-zone.

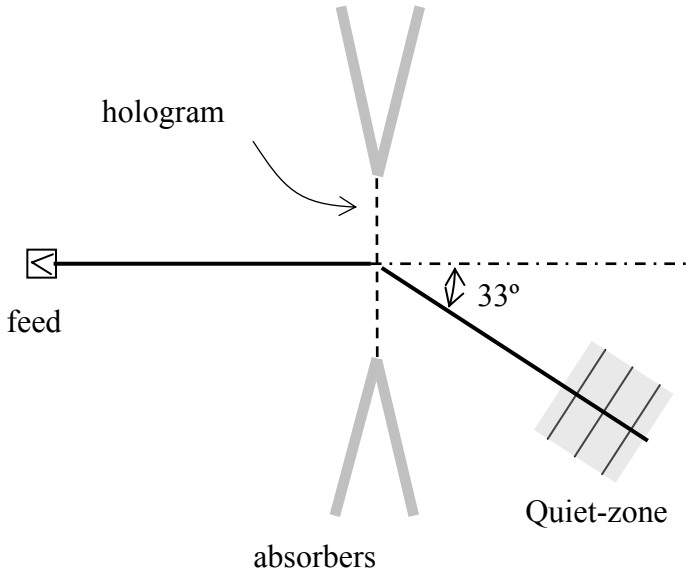

Figure 2.2 Schematic layout of a hologram-based CATR.

The hologram pattern is etched on a metal layer on a thin Mylar film. The pattern consists of vertical, slightly curved slots in the copper-laminate. Because of the planar structure and because the hologram is a transmission type element, the manufacturing accuracy requirement is not as high as for reflectors. A hologram is light weight and inexpensive device compared to other types of collimating elements in CATRs.

A hologram-based CATR has been used for antenna testing at the frequencies up to 322 GHz. A 1.5 metre diameter antenna was measured at 322 GHz in 2003. The design and construction of the CATR is presented in [Lönnqvist 2005] and antenna test results in [Häkli 2005b].

A transmission-type hologram can be an amplitude hologram or a phase hologram. In an amplitude-type hologram the radiation is partially blocked by metal strips and partially transmitted through slots between the metal strips. A phase hologram is based on locally

varying the effective electrical path length, for example by varying the effective thickness pattern. A phase hologram can be realized by milling grooves on a dielectric substrate [Lönnqvist 2003], [Räisänen 2003a]. With a phase hologram it is possible to have higher conversion efficiency, i.e., lower losses. A phase hologram has been used in a hologram-based compact radar cross section (RCS) range for scale model measurements at 310 GHz [Lönnqvist 2003], [Räisänen 2003a]. The layout of the RCS range is similar to the layout in Figure 2.2. The scale model is placed in the QZ and the transmitter and receiver are separated with a dielectric slab working as a directional coupler.

A reflection-type phase hologram for CATR has also been designed [Noponen 2006]. In a reflection-type phase hologram grooves are milled into a metal slab. The main advantages compared to transmission-type holograms are lower losses and that the harmful reflections inside the hologram are avoided.

2.2.1 Design of the hologram

A transmission-type hologram can be designed with electromagnetic simulations [Hirvonen 1997], [Ala-Laurinaho 1997]. The structure of the hologram is analysed with finite-difference time-domain method (FDTD) and the quiet-zone field is calculated with physical optics (PO) from the aperture field. Because the whole hologram is too large to simulate only one cut of the nonuniform metal grating is analysed [Ala-Laurinaho 1997]. The analysed structure is illustrated in Figure 2.3.

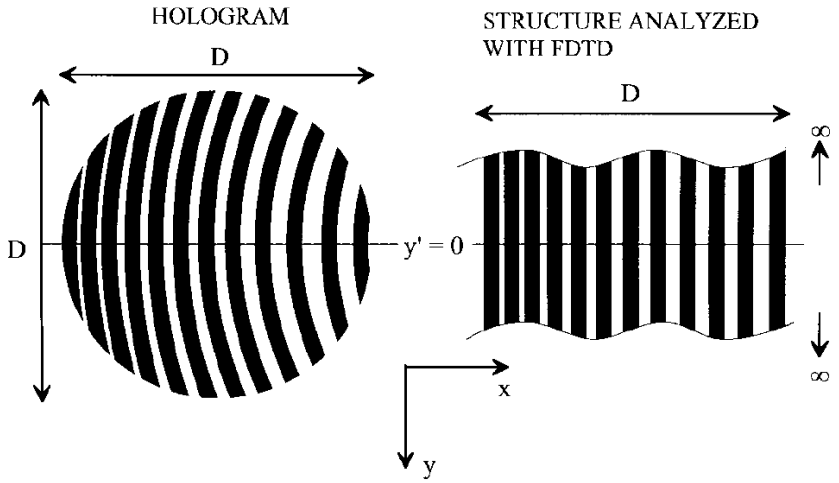

Figure 2.3 Structure analysed with FDTD [Hirvonen 1997].

The hologram structure is calculated from a binarized interference pattern of the input and output fields. The location of the slots affects the phase and the width affects the amplitude. The structure is optimized based on the simulated quiet-zone field.

An example of a hologram pattern is in Figure 2.3. The amplitude has to be tapered toward the edge to avoid edge diffractions. The amplitude tapering can be done by narrowing the slots towards the edges of the hologram.

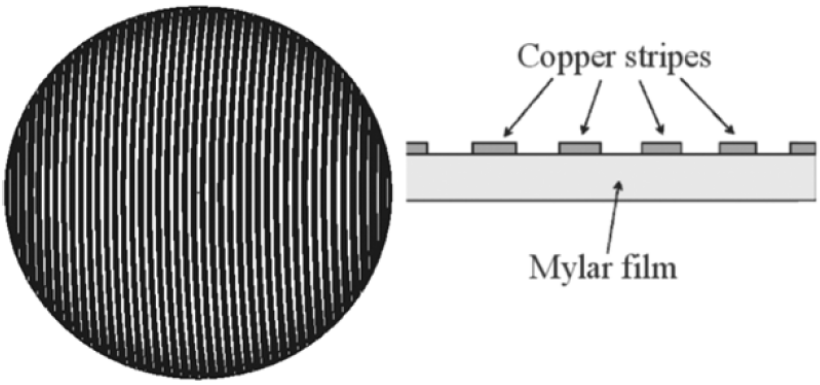

Figure 2.4 An example of a hologram pattern [Häkli 2005b].

2.2.2 DRFS for hologram-based CATR

Traditionally a corrugated feed horn has been used to illuminate the hologram. This leads to high edge illumination of the hologram and the slots need to be narrowed towards the edges to reduce the ripple caused by edge diffractions. Because transmission of a horizontal polarization through the vertical slots is nearly independent of the slot width, edge diffraction at the horizontal polarization is not avoided with the narrowing of the slots. This limits the use of a hologram to the vertical polarization. The narrow slots are also difficult to manufacture accurately.

A dual reflector feed system (DRFS) can be used to modify the hologram illumination [Häkli 2004], [Häkli 2005c]. With amplitude tapering towards the edges of the hologram in the hologram illumination the narrow slots are avoided in the hologram pattern. As the narrow slots are avoided hologram can be designed to operate also at the horizontal polarization and also cross-polarization performance is improved as wider slots cause less cross-polarization. By using the DRFS as a feed cross-polarization performance of the hologram is improved by about 10 dB [Ala-Laurinaho 2006]. The generated cross-polar

component depends on the transmission difference between vertical and horizontal polarizations and on the slot direction deviation from vertical direction. The transmission difference is larger for narrow slots which can be avoided when DRFS is used.

The DRSF is used to generate spherical wave-front with flat amplitude in the centre of the beam and amplitude tapering towards the edge of the hologram. As the DRFS is largely responsible for the amplitude modification, the -1 dB beam width of the DRFS determines the QZ size. The QZ diameter is approximately cos(33°) times the -1 dB beam width in the horizontal direction.

2.3 Hologram-based compact antenna test range at 650 GHz

MilliLab/Radio Laboratory at TKK is developing a 650 GHz hologram-based compact antenna test range [Ala-Laurinaho 2006]. A 1.5 metre antenna will be tested at 650 GHz in 2006. As a part of this project a 650 GHz dual reflector feed system has been designed and it will be used in the CATR. The design of this DRFS is the subject of this thesis.

The test object will be Planck Radio Frequency Qualification Model (RFQM) or ADMIRALS RTO (Representative Test Object). Both have a main reflector diameter about 1.5 metres. The ADMIRALS RTO has been measured at 322 GHz in a hologram-based compact antenna test range at TKK [Lönnqvist 2005], [Häkli 2005b].

Layout of the test range will be as indicated in Figure 2.2. The hologram diameter is 3.18 metres, the focal length of the hologram is 12.72 metres and the distance from the centre of the hologram to the antenna under test (AUT) 9.6 metres. The ratio between the focal length and the diameter of the hologram has been increased from 3 to 4. This makes the slots in the hologram more uniform in width and thus in principle decreases the cross-polarization in the quiet-zone by about 3 dB [Ala-Laurinaho 2006]. The possibility to decrease the offset angle from 33° to 25° is considered as that would increase the quiet-zone by about 8% in the horizontal direction [Ala-Laurinaho 2006].

The desired hologram illumination was decided to have a -1 dB beam width 75% of the hologram radius (1190 mm), corresponding to a 2 metre wide quiet-zone. The hologram edge illumination was decided to be under -10 dB, the ratio between the hologram focal

length and the diameter of the hologram f_{holo}/D_{holo} = 4 and amplitude ripple less than 0.7 dB peak-to-peak and deviation from a spherical phase less than 7° peak-to-peak. The size of the reflectors and the size of the feed system should be kept moderate.

Currently the maximum size of a hologram piece is limited, so the 3.18 metre hologram is made from three pieces that are joined by soldering. The hologram is manufactured by chemical wet etching on a 50 μm thick Mylar film. The feasibility of hologram CATR for higher sub-millimetre frequencies has been studied and two demonstration holograms have been designed and measured at 644 GHz [Koskinen 2005].

The quality of the quiet-zone is measured with a plane-polar-type quiet-zone scanner. The quiet-zone is optimized by finding the optimal location for the feed system. Feed scanning [Viikari 2005] and frequency shifting method based methods are the possible pattern correction techniques. The DRFS is mounted on a feed positioner so that it can be moved accurately. The size of feed system should stay moderate so that it does not become too heavy for the positioner.

3 Reflector antennas

Reflector antennas are widely used in telecommunication applications, radars, radio astronomy and compact antenna test ranges. Usually high-gain antennas are reflector antennas. Reflector antennas are secondary radiators, which redirect the radiation of the primary source, the feed. The feed is usually a small horn antenna. Also feed arrays can be used. Reflector antenna has usually one or two reflectors.

Many factors have to be taken into account in designing a reflector antenna. The radiation pattern is affected for example by: the radiation pattern of the feed, shape of the reflector, diffraction, spillover, multiple reflections, depolarization, aperture blockage, errors in positioning of the feed or the reflector, and the reflector surface accuracy. For example small random surface errors affect the aperture efficiency [Räisänen 2003b]:

$$\eta_{ap} = \eta_0 e^{-\left(\frac{4\pi\varepsilon}{\lambda}\right)^2}, \tag{3.1}$$

where η_0 is the aperture efficiency of the ideal surface, ε is the root mean square surface error and λ is the wavelength. The surface accuracy is proportional to wavelength and thus may limit the maximum usable frequency of the reflector.

Basic antenna geometries are presented in Section 3.1. Shaped reflector antennas are presented in Section 3.2. In Section 3.3, the radiation analysis methods used in the design of the DRFS are described. Reflector antenna geometries and analysis of their radiation is explained in literature, for example in [Collin 1985], [Lindell 1997].

3.1 Basic reflector antenna geometries

The most common basic geometry for a reflector antenna is based on a paraboloid surface. A paraboloid collimates the radiation coming from a focal point, i.e., transforms a spherical wave to a plane wave. Because of this geometrical property, paraboloidal reflector antennas are widely used for high gain antennas for example in communication applications. The paraboloid can be fed directly from the focal point or a subreflector antenna can be used whose focal point coincides with the focal point of the paraboloid. If the subreflector is a hyperboloid the dual reflector system is called a Cassegrain antenna and a Gregorian antenna if the subreflector is elliptical. Cassegrain geometry is more

common because the structure is more compact. Figure 3.1 a) shows a Cassegrain antenna fed from the vertex of the paraboloid.

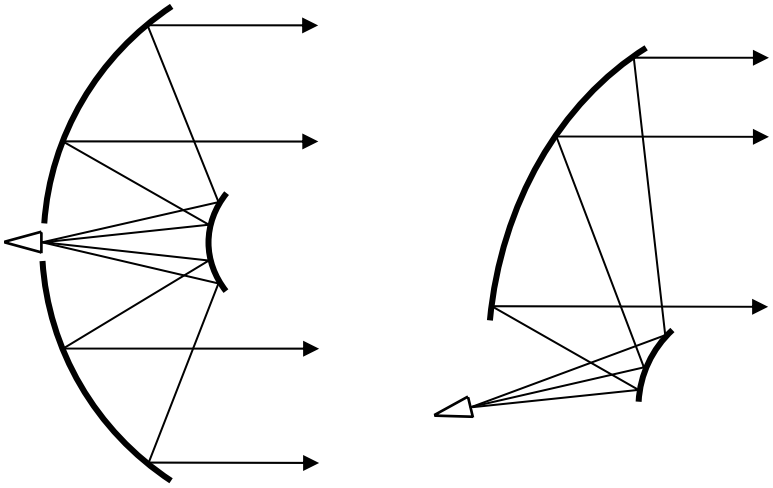

a) b)

Figure 3.1 Basic reflector antenna geometries: a) a front-fed Cassegrain antenna, b) an offset Cassegrain antenna.

Because of the aperture blockage and scattering from the support structure of the feed or the subreflector low side lobe level and low cross-polarization are difficult to obtain. An offset structure can be used to avoid aperture blockage and also to avoid multiple reflections between feed and reflectors. Figure 3.1 b) shows an offset Cassegrain antenna. The penalty of using an offset geometry is increased cross-polarization. The cross-polarization level is typically -20 to -25 dB for a single offset reflector [Collin 1985].

The cross-polarization caused by the offset structure can be minimized with so called compensated design that is based on the Mizugutch condition [Mizugutch 1976]. The Mizugutch condition is based on choosing the angles between subreflector and main reflector and the subreflector eccentricity. Similar condition for dual hyperboloid or elliptical reflector antennas has been derived [Luh 1997].

Also a spherical main reflector can be used. A spherical surface is easier to manufacture accurately than a paraboloid. A spherical surface does not have a focal point, but radiation can be directed to a single point with a subreflector. Spherical reflectors are commonly used in applications where beam scanning is needed as spherical reflectors are not so sensitive to feed movement as paraboloid and thus allow a larger scanning angle.

The world's largest reflector antenna in Arecibo has a spherical main reflector and it allows a scanning angle of 11° at 1.415 GHz [Lindell 1997].

Elliptical or hyperbolical reflector can be used to move the focal point. A spherical wave originating from the focal point is transformed to a spherical wave originating from the other focal point after reflection from the surface. Elliptical and hyperbolical surfaces and their focal points are illustrated in Figure 3.2. Ellipsoids and hyperboloids are used as subreflector in Cassegrain and Gregorian antenna geometries. Also both of the reflectors in a dual reflector antenna can be ellipsoids and hyperboloids.

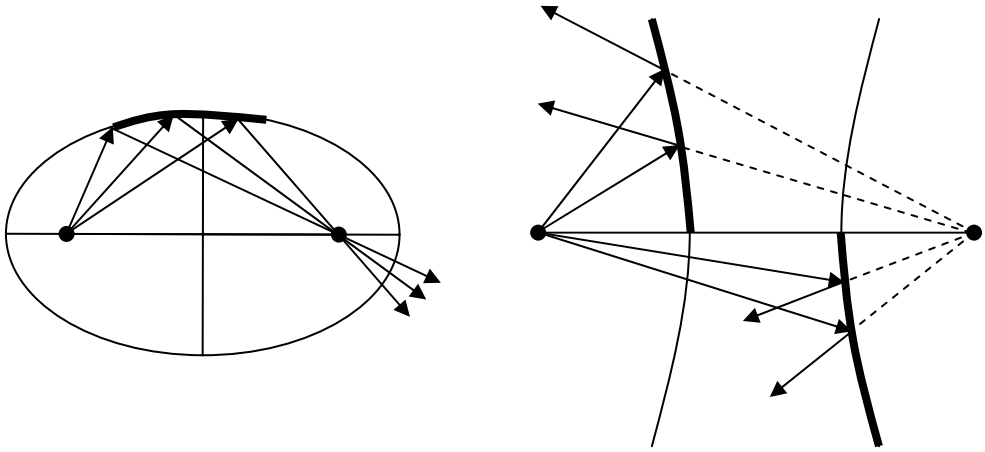

a) b) c)

Figure 3.2 a) Elliptical surface b) concave hyperbolic surface c) convex hyperbolic surface.

Paraboloid, sphere, hyperboloid and ellipsoid can all be expressed with the following equation [Lindell 1997]:

$$r(\theta) = \frac{(1+e)f}{1+e\cdot\cos(\theta)}, \tag{3.2}$$

where e is eccentricity and f is the focal length (or radius). For a sphere $e = 0$, an ellipsoid $e < 0$, a paraboloid $e = 1$, a hyperboloid $e > 0$ and for a plane $|e| \to \infty$.

3.2 Shaped reflector antennas

The reflector antenna performance can be improved by shaping the reflector or reflectors. A constant aperture field results in high gain and high side lobe levels. By shaping the reflector it is possible to realize amplitude tapering to the aperture field and thus get

lower side lobe levels. Shaping can also be used to get more uniform aperture distribution, which increases the efficiency and increases gain. In general, shaping of a single reflector does not enable both amplitude and phase to be varied independently. With a dual reflector antenna, in which both reflectors are shaped, both amplitude and phase can be modified. In practice the subreflector is shaped to modify the amplitude and the main reflector is shaped to correct the phase distribution. This is because a same size variation in shape of the smaller subreflector results in a larger change of the amplitude. The shape of the larger main reflector does not affect the amplitude as much as it affects the path length and the phase.

Shaped reflector antennas are based on some basic geometry. The reflectors are shaped to achieve the desired property, i.e., such as for example the shape or size of the reflectors, desired edge illumination, minimal cross-polarization, nulls to desired directions, side lobe level or desired output beam shape. The design goal depends on the application. For example satellite broadcasting antennas are shaped to modify the beam shape so that it corresponds to the shape of the geographical service area. These antennas are usually called contoured-beam antennas. For search radar the beam should be narrow in horizontal and wide in vertical direction.

Calculating the reflector surfaces from the initial parameters is called reflector synthesis. Reflector synthesis methods are discussed in Chapter 4. The synthesis method used in the design of the DRFS for hologram-based CATR is explained in Section 4.3.

3.2.1 Dual reflector feed system

A feed system is designed to give desired illumination for main reflector of reflector antenna or the collimating element of a compact antenna test range. The additional degrees of freedom given by shaped dual reflector feed system can be used, for example, to give more uniform aperture distribution or to realize amplitude tapering to avoid edge diffractions. A shaped dual reflector feed system can be used to improve reflector-based CATR as described in [Descardeci 1997], where designing of a dual reflector feed system for a CATR based on a single-offset paraboloidal reflector is described.

A dual reflector feed system (DRFS) can be used to improve hologram-based compact antenna test range (CATR). A 310 GHz DRFS for hologram CATR has been designed

[Häkli 2004], [Häkli 2005c]. It consists of two shaped hyperboloid reflectors, a concave subreflector and convex main reflector. The DRFS is used to realize a spherical wave with flat amplitude in the centre of the output beam and amplitude tapering towards the hologram edges. The design of a similar feed system for a 650 GHz hologram-based CATR is the subject of this thesis.

3.3 Analysis of the reflector antenna radiation

In this section the antenna radiation analysis methods used in the design of the DRFS are described. Geometrical optics (GO) is used in the synthesis of the reflector surfaces. The synthesis method is described in Section 4.3. Physical optics (PO) and physical theory of diffraction (PTD) are used in the simulations described in Chapter 5.

3.3.1 Geometrical optics

Geometrical or ray optics is widely used in design of electrically large lens and reflector antennas. The theory is explained for example in [Collin 1985] (in English) or in [Lindell 1997] (in Finnish).

Geometrical optics is a high frequency approximation of the Maxwell equations. The fields can be expanded as power series of inverse powers of the angular frequency ω [Lindell 1997]

$$\overline{E}(\omega,\bar{r}) = e^{-jk_0 L(\bar{r})} \sum_{i=0}^{\infty} \frac{\overline{E}_i(\bar{r})}{(j\omega)^i}, \tag{3.3}$$

$$\overline{H}(\omega,\bar{r}) = e^{-jk_0 L(\bar{r})} \sum_{i=0}^{\infty} \frac{\overline{H}_i(\bar{r})}{(j\omega)^i}, \tag{3.4}$$

where $L(\bar{r})$ is the so called eikonal function and $k_0 = \omega\sqrt{\mu_0\varepsilon_0}$. At the high frequencies the 0^{th} order dominates [Lindell 1997]

$$\overline{E}(\bar{r}) \approx \overline{E}_0(\bar{r}) e^{-jk_0 L(\bar{r})}, \tag{3.5}$$

$$\overline{H}(\bar{r}) \approx \overline{H}_0(\bar{r}) e^{-jk_0 L(\bar{r})}. \tag{3.6}$$

This is called the geometrical optics approximation. For an eikonal function the eikonal equation can be written [Lindell 1997]:

$$\nabla L(\bar{r}) \times \nabla L(\bar{r}) = \mu_r(\bar{r})\varepsilon_r(\bar{r}) = n^2(\bar{r}), \tag{3.7}$$

where $n(\bar{r}) = \sqrt{\mu_r(\bar{r})\varepsilon_r(\bar{r})}$ is the index of refraction of the medium.

3.3.1.1 Local plane wave

The Maxwell equations can be written with the 0^{th} order components of the power series in (3.3) and (3.4) as [Lindell 1997]

$$\bar{k}(\bar{r}) \times \overline{E}_0(\bar{r}) = \mu_0(\bar{r}) k_0 \eta_0 \overline{H}_0, \tag{3.8}$$

$$\bar{k}(\bar{r}) \times \overline{H}_0(\bar{r}) = -\frac{\varepsilon_r(\bar{r}) k_0}{\eta_0} \overline{E}_0, \tag{3.9}$$

where $\bar{k}(\bar{r})$ is the local wave vector:

$$\bar{k}(\bar{r}) = k_0 \nabla L(\bar{r}). \tag{3.10}$$

Equations (3.8) and (3.9) describe a plane wave field. In lossless medium, the geometrical optics field vectors $\overline{E}_0(\bar{r})$, $\overline{H}_0(\bar{r})$ and $\bar{k}(\bar{r})$ are perpendicular to each other and the surface where the phase is constant is given by the surface where L is constant. For lossless medium where the eikonal function is real, the Poynting vector is [Lindell 1997]

$$\overline{S}_0 = \frac{1}{2}\overline{E}_0 \times \overline{H}_0^* = \frac{1}{2\mu_r k_0 \eta_0} \bar{k} \left| \overline{E}_0 \right|^2. \tag{3.11}$$

It can be seen from (3.11) that power propagates in the direction of $\bar{k}$, i.e., perpendicular to the constant phase front.

3.3.1.2 Ray path

In geometrical optics ray vectors are used to represent the fields. The ray equation represents the direction of propagation. For a ray $\bar{r}(s)$ the ray equation derived from the eikonal equation is [Lindell 1997]:

$$\bar{t} \cdot \nabla(n\bar{t}) = \frac{d}{ds}\left(n(\bar{r}) \frac{d\bar{r}}{ds} \right) = \nabla n(\bar{r}), \tag{3.12}$$

where $\bar{t}$ is the tangential unit vector of the ray and s is the distance along the ray. The ray equation is a second order non-linear differential equation. It can be solved analytically

for some cases, but usually it is solved numerically. For homogenous medium $n(r) = n$ Equation (3.12) can be solved simply [Lindell 1997]

$$\frac{d^2\bar{r}(s)}{ds^2} = 0 \quad \Rightarrow \quad \bar{r}(s) = \bar{t}_0 s + \bar{r}_0 , \tag{3.13}$$

where the original direction $\bar{t}_0$ and the position $\bar{r}_0$ are constants. Ray in a homogenous medium is a straight line.

3.3.1.3 Amplitude along the ray

From the ray equation the ray path can be calculated but not how the field changes along the ray, i.e., as the function of s. Field amplitude is calculated from the transport equation [Lindell 1997]:

$$\frac{d\bar{E}_0}{ds} = -\frac{1}{n}\bar{t}(\nabla n)\cdot\bar{E}_0 - \frac{\mu_r}{2n}\nabla\cdot(\bar{t}\frac{n}{\mu_r})\bar{E}_0 . \tag{3.14}$$

The transport equation is a differential equation for an unknown vector $\bar{E}_0$. If $\bar{E}_0$ is known at some point it can be solved at all points along the ray. It can be proved from (3.14) that $\left|\bar{E}_0\right|^2$ integrated over the cross section of a ray tube is constant. Usually the ray tube is defined as the space between four adjacent rays. Power propagates inside the ray tube and the power density depends on the cross sectional area of the ray tube. Also polarization along the ray can be calculated from (3.14). For a straight ray the polarization does not change along the ray.

3.3.1.4 Phase of the ray

The ray length corresponds to the phase of the field. Ray length s in the ray direction corresponds to phase $-ks$, i.e. phase decreases along the ray in the direction of propagation, so that in a homogenous lossless medium distance of one wavelength corresponds to a phase change of -360°. If the complex time factor for positively travelling wave would be written as $e^{i\omega r}$, instead of $e^{-j\omega r}$, the phase would increase.

3.3.1.5 Surface and wave front curvature parameters

In general, a wave front, i.e. constant phase surface, has a local expansion defined by two principal radii of curvature R_1 and R_2 and principal directions of curvature $\bar{\kappa}_1$ and $\bar{\kappa}_2$. The curvature parameters are illustrated in Figure 3.3. Same kind of local expansion can

be used for surfaces. The curvature parameters can be traced along the rays and calculate how they change in reflection or transmission.

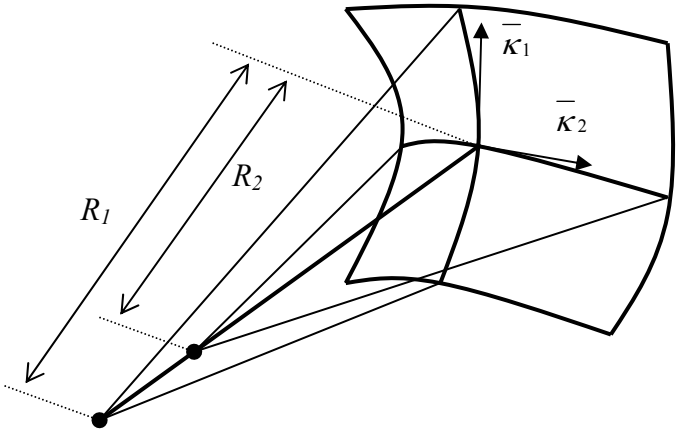

Figure 3.3 The two principal radii of curvature.

The local expansion of the surfaces can be done in many different ways. For example in [Kildal 1990], wave fronts and reflector surfaces are approximated with bi-parabolic expansions. In the synthesis method used in the design of the DRFS, as explained in Section 4.3, wave fronts and reflector surfaces are approximated with planes, which simplify the calculations.

3.3.2 Physical optics

In physical optics (PO) surface currents are calculated from the incident and reflected fields from the surface currents. In PO, the surface is assumed locally flat and infinite. Surface current density on a perfect electric conductor is [Pontoppidan 2003]

$$\bar{J}_e = 2\bar{n} \times \bar{H}_i, \tag{3.15}$$

where $\bar{n}$ is the surface normal and $\bar{H}_i$ is the incident magnetic field. In the shadow region, i.e., surface area that is not directly illuminated by the incident fields, the surface currents are assumed to be zero.

The surface currents are calculated in discrete points on the antenna surface. At the surface current points the surface is approximated with the tangential plane and surface current is calculated from (3.15). In order to get sufficient accuracy with this approximation the dimensions and radius of curvature have to be at least a few wavelengths. The number of current elements has to be large enough for the PO to give

accurate prediction of the reflected field. The required number of the elements depends on the size and the shape of the object compared to the wavelength and the desired field accuracy.

3.3.3 Physical theory of diffraction

Physical theory of diffraction (PTD) can be used to include edge diffractions to PO [Pontoppidan 2003]. In PTD edge currents are calculated from the shape of the edge and the incident field. The field calculated from edge current is added to PO fields

$$\overline{E} = \overline{E}_{PO} + \overline{E}_{PTD} . \tag{3.16}$$

In the edge current calculations the edge is approximated locally to be a perfectly conducting half plane [Pontoppidan 2003]. The radius of curvature of the edge and the number of current elements has to be sufficiently large for this approximation to be valid.

4 Reflector synthesis methods

The first reflector synthesis methods were developed in the 1940's. The reflector synthesis means that the reflector surfaces are calculated by some means from known feed radiation and desired radiation of the reflector antenna. The synthesis methods can be divided into two groups, to direct and indirect methods. In indirect methods the aperture field of the antenna is calculated from the desired far-field and the reflectors are synthesized to produce this aperture field. The direct methods use the desired far-field in the reflector synthesis.

The synthesis methods can be divided also by the method used to compute the radiation. The geometrical optics based methods use geometrical optics (GO) and the diffraction synthesis methods usually use physical optics (PO) and usually also physical theory of diffraction (PTD). Examples of the synthesis methods are presented in this chapter.

4.1 Diffraction synthesis methods

The diffraction synthesis methods are based on PO and usually also diffraction is included with PTD. Several diffraction synthesis methods have been developed. An example of an indirect PO-based method is described in [Westcott 1993], where GO is used to calculate the aperture field and PO in the synthesis to optimize desired gain at a number of points. Example of direct PO-based synthesis is in [Bergmann 1988]. A generalized diffraction synthesis technique is described in [Duan 1995], where the synthesis method combines optimization procedures, physical optics (PO) and diffraction analysis with physical theory of diffraction (PTD). The synthesis is generalized for single- and dual-reflector antennas fed by either a single feed or an array feed. Another direct PO-based method is presented in [Hay 1999], in which successive projections method is used, i.e., iterative process where the reflector surfaces are changed until the design constraints are satisfied.

4.2 Geometrical optics based synthesis methods

In the geometrical optics based synthesis methods geometrical optics (GO) is used to calculate the radiation, i.e., Snell's law at reflections, phase dependence on the ray length and conservation of energy in the flux tubes. The mathematical problem of synthesizing a

dual reflector antenna with geometrical optics was first solved for a rotationally symmetric case in the 1960's. An example of a synthesis method for rotationally symmetric antennas is in [Galindo 1964]. Synthesis methods for offset dual reflectors have been developed [Hoerner 1978], [Westcott 1981], [Bjøntegaard 1983]. The synthesis methods have been extended for elliptical apertures, for example [Albertsen 1985].

The geometrical optics synthesis methods are usually based on solving partial-differential equations. A synthesis method that simplifies the synthesis problem to solving ordinary linear equations is presented in [Kildal 1990]. This simplification of the problem has been possible by using the so called ray tracing [Kildal 1990]. Reflector surfaces and wave-fronts are described in terms of curvature parameters of the bi-parabolic expansions. The rays originating from the feed are mapped to ellipses in the output aperture with the law of conservation of power. To get the mapping exact extra variables are added to the mapping, i.e., by allowing the radial lines of the aperture ray grid to be curved. Rays are traced from feed to the subreflector and from the aperture to the main reflector. The reflector points are the interception points of the rays and the surfaces of the local bi-parabolic expansions in the closest known reflector points. The reflector curvature parameters are calculated from the known ray path.

The synthesis method in [Kildal 1990] has been simplified by assuming that the reflector surfaces and the wave-fronts are locally planar and by using rotationally symmetric mapping [Häkli 2004], [Häkli 2005a]. The assumption of rotational symmetry in mapping, in practice, means that the feed horn radiation pattern is assumed to be rotationally symmetric. The error caused by the symmetry assumption is neglected in the synthesis method. This numerical synthesis method is described in detail in Section 4.3 and used in the design of the 650 GHz DRFS. The reflector surfaces have also been approximated with planar sections for example in [Descardeci 1997], [Rubiños-López 1997].

4.3 Numerical synthesis method for designing a dual reflector feed system

A numerical synthesis method is described in [Häkli 2004], [Häkli 2005a]. The synthesis method was developed specifically for designing a dual reflector feed system (DRFS) for

hologram-based compact antenna test range (CATR) [Häkli 2005c]. The synthesis is a direct ray-tracing-based synthesis procedure, that is based on the method described in [Kildal 1990] with some simplifications. In the synthesis the electromagnetic fields are represented with rays that represent the local plane wave amplitude and phase. The reflector surfaces are approximated with locally planar sections.

The synthesis of the feed system starts with defining the basic geometry. Then input and output fields and rays are defined. Finally, the reflector surfaces are synthesised and the reflector edges are rounded.

4.3.1 Basic geometry

The basic geometry of the dual reflector feed system is shown in Figure 4.1. The feed system is not in scale and the reflector sizes are exaggerated. The feed horn location is defined by the feed horn phase centre point and the feed angle α_{feed}. The first reflector is called subreflector and the second main reflector. The focal length of the subreflector f_{sub} is the distance between feed horn phase centre point and the subreflector. Subreflector offset angle is α_{sub} and distance between the reflectors is r_{sub}. The focal point of the hologram is F_{holo}. The diameter of the hologram is D_{holo}. The focal length of the system is f_{holo} and the distance from main reflector to the hologram centre point is r_{main}. The solid line in Figure 4.1 is the centre ray path. The centre ray path length is equal to the hologram focal length [Häkli 2005a]

$$f_{holo} = f_{sub} + r_{sub} + r_{main} . \tag{4.1}$$

The basic geometry of the DRFS is a dual hyperboloid reflector. The subreflector focal points are the feed horn phase centre point and the common focal point of the subreflector and the main reflector behind the subreflector, i.e., in Figure 4.1, point from where the rays from the subreflector to the main reflector appear to originate. The second focal point of the main reflector is the hologram focal point F_{holo}. The surfaces are shaped surfaces without clear focal points, but they can be called shaped hyperboloids because they can be considered to have focal regions centred around those focal points. The subreflector is concave and the main reflector is convex.

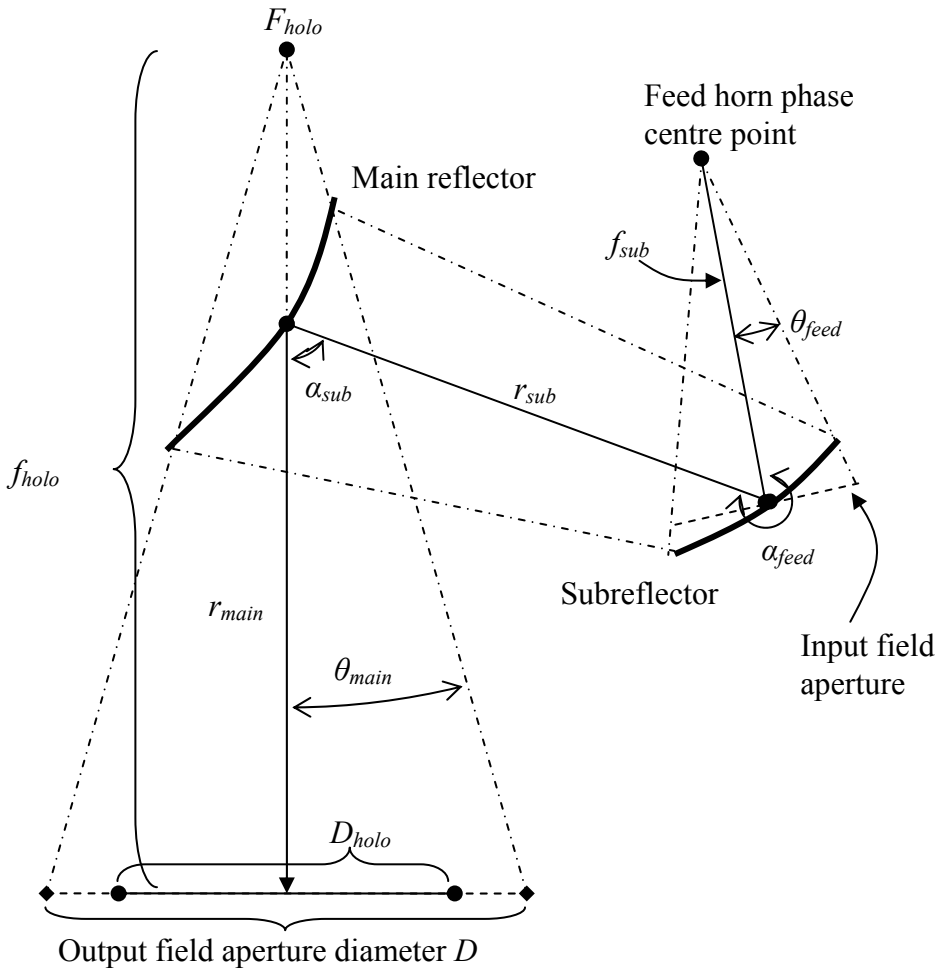

Figure 4.1 Basic geometry of the DRFS.

4.3.1.1 The coordinate systems

Four coordinate systems are used to define the structure and the fields. The coordinate systems are: the global coordinate system, the feed horn coordinate system, the subreflector coordinate system, and the main reflector coordinate system. The origin of the global coordinate system is in the hologram focal point F_{holo}. The coordinate systems are defined by the location of the origins in the global coordinates and by the angles β_{feed}, β_{sub} and β_{main}, i.e., the angles between their z-axis and the global z-axis. The coordinate system definitions are shown in Figure 4.2.

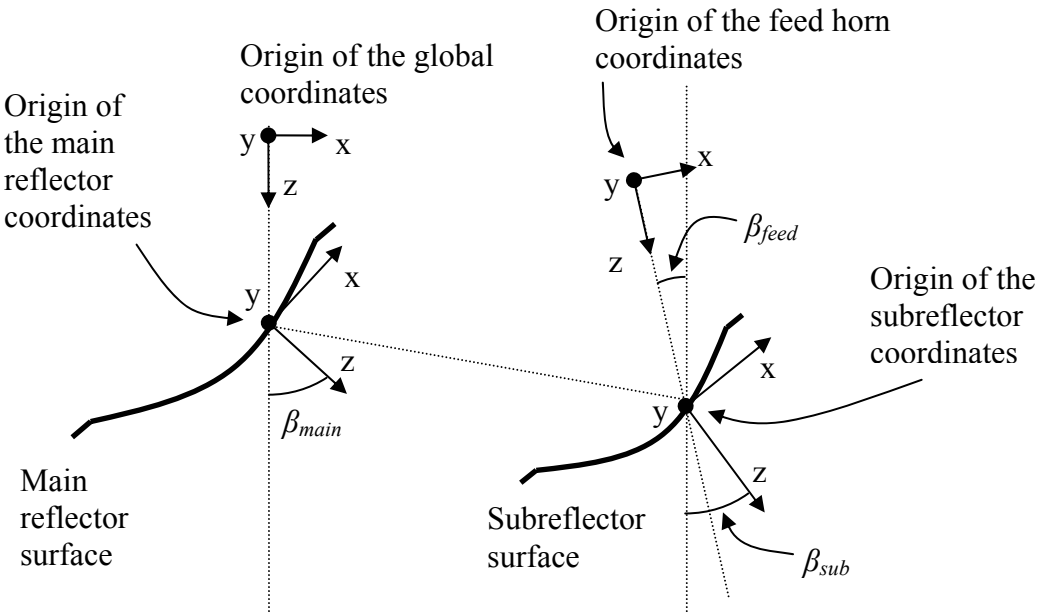

Figure 4.2 The coordinate system definitions.

The feed horn location and the feed horn radiation pattern are defined in the feed horn coordinates. The subreflector coordinates and main reflector coordinates are used to define the reflector surfaces. Two aperture planes are used to define input and output fields. The input field aperture and the output field aperture are shown in Figure 4.1. The input field aperture is a plane $z = f_{sub}$ in the feed horn coordinates. The output field aperture is a plane $z = f_{holo}$ in the global coordinates.

4.3.2 Representation of fields with rays

The electromagnetic fields are represented with rays. A ray represents the local plane wave perpendicular to the ray direction. The ray grid is defined in polar coordinates as illustrated in Figure 4.3. The ray grid is $N \times M$ matrix with N rings and M rays on each ring. The first ring is formed by M rays in the centre of the grid and the rays at $\phi = 0^{\circ}$ are duplicated at $\phi = 360^{\circ}$. Flux tubes are formed by four adjacent rays. The flux tubes are numbered so that tube *(n,m)* is cornered by rays *(n,m), (n,m+1), (n+1,m)* and *(n+1,m+1)*.

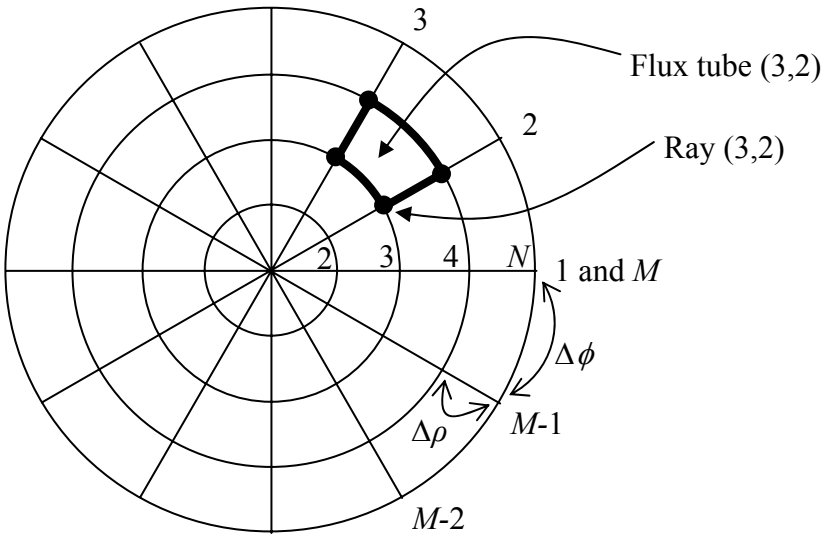

Figure 4.3 Ray grid and flux tubes.

Each ray has electric field amplitude E that is interpolated from the vertical polarization of the feed horn radiation data. The length of the ray corresponds to the phase of the ray so that one wavelength is 360º in the phase. Power is assumed to propagate in the flux tubes. The flux tube power is computed from the real part of the Poynting vector by using the average of the electric field amplitudes of the corner rays and the surface area of the tube *dA(n,m)* [Häkli 2005a]

$$P(n,m) = \frac{1}{2}\mathrm{Re}\left\{ \int_{s(n,m)} \overline{E} \times \overline{H}^{*} \cdot d\overline{S} \right\} \approx \frac{1}{2\eta} E_{ave}^{2}(n,m) dA(n,m)\,, \tag{4.2}$$

where η is the free-space wave impedance and

$$E_{ave}(n,m) = \frac{1}{2}(E_{n,m} + E_{n,m+1} + E_{n+1,m} + E_{n+1,m+1})\,. \tag{4.3}$$

4.3.3 Input field definition and representation with rays

The input ray amplitudes are interpolated from the vertical polarization of the radiation pattern of the feed horn. The input rays are defined so that they originate from the feed horn phase centre point and intersect the input field aperture plane at points in a constant angular and radial polar grid, i.e., a grid with constant $\Delta\phi$ and constant $\Delta\rho$. The feed horn phase centre point and the input field aperture plane are shown in Figure 4.1. The phase of the feed horn is neglected in the synthesis.

4.3.4 Output field definition and output rays

The output field is defined in the output field aperture plane at constant angular and constant radial polar grid at $N \times M$ discrete points. The output field is computed from a rotationally symmetric Butterworth-type function

$$E(\rho') = \frac{1}{\sqrt{1+(\rho'/\rho_c)^{2N}}}, \tag{4.4}$$

where ρ_c and N are the -3 dB point and the degree of the Butterworth function and ρ' is the output field aperture coordinate. The output rays originate from the hologram focal point F_{holo} and end in the output field aperture plane. The output ray amplitudes are calculated from (4.4) in the output field aperture in the constant angular and constant radial polar grid. The desired output field phase is a spherical phase originating from the hologram focal point. The output field phase is modified by adjusting the total lengths of the rays.

4.3.5 Rotationally symmetric aperture mapping

The input rays are mapped to the output rays, i.e., the output ray amplitudes and the output ray grid are changed so that the power in each ray tube is the same in the output ray tube as in the corresponding input ray tube. The mapping assumes rotationally symmetric fields, i.e., the input field is averaged

$$E_{in}(n) = \frac{\sum_{m=1}^{M-1} E_{in}(m,n)}{M-1}. \tag{4.5}$$

The ray ring power is

$$P_{in}(n) = \frac{1}{2\eta}\frac{E_{in}(n+1)+E_{in}(n)}{2}\left(\pi\rho_{n+1}^2 - \pi\rho_n^2\right). \tag{4.6}$$

The mapping is done in two parts, first the amplitudes of the output rays are scaled to make the total output power equal to the total input power and then the new output field aperture coordinates are calculated so that the power is equal for each ray ring, i.e.,

$$P_{in}(n) = P_{out}(n). \tag{4.7}$$

The input ray amplitudes and the output ray amplitudes have been normalized so that the peak values are set to one. The normalized output ray amplitudes $E_{norm}(n)$ are scaled so

that the total power of the output flux tubes is equal to the total power of the input flux tubes. The scaling factor α is

$$\alpha = \frac{\sum_{n=1}^{N-1} P_{in}(n)}{\sum_{n=1}^{N-1} P_{norm}(n)}, \tag{4.8}$$

where $P_{in}(n)$ and $P_{norm}(n)$ are solved with (4.6), using $E_{in}(n)$ and $E_{norm}(n)$, respectively. The output ray amplitudes are scaled

$$E_{out}(n) = \sqrt{\alpha} E_{norm}(n). \tag{4.9}$$

The new output field aperture coordinates are calculated so that the power is equal in each ray ring. The input power for each ray ring is known from (4.6). The output field $E_{out}(n)$ is known in a constant $\Delta\rho'$ grid. The power density is approximated to be a linear function between the known points, i.e., when $\rho'_n \le \rho' \le \rho'_{n+1}$

$$E_{out}^2(n) = k_n \rho' + b_n, \tag{4.10}$$

where k_n and b_n are calculated from $E_{out}(n)$ and $E_{out}(n+1)$. The new ρ' coordinates are calculated starting from the centre of output field aperture by solving ρ'_{n+1} from

$$P_{in}(n) = P_{out}(n) = \frac{1}{2\eta} \int_{\rho'_n}^{\rho'_{n+1}} E_{out}^2(\rho') 2\pi\rho' d\rho', \tag{4.11}$$

where $E_{out}^2(\rho')$ is a piece-wise continuous function calculated using (4.10).

The output rays originate from the hologram focal point F_{holo} and end to the output field aperture grid that has constant $\Delta\phi'$. The ρ'-coordinates are calculated from (4.11).

4.3.6 Synthesis of the reflector surfaces

The reflector surfaces are synthesized from the known input and output rays and from the geometry of the feed system by tracing the rays, using the Snell's law for reflections and ray length adjustment. The reflector surfaces are assumed locally planar.

The known information in the beginning of the synthesis is illustrated in Figure 4.4. The centre ray is known from the basic geometry shown in Figure 4.1. The centre ray interception points on the reflectors are the first known points in the reflector surfaces

and the origins of the subreflector and main reflector coordinates. The origins and the end points of the input and output rays are also known.

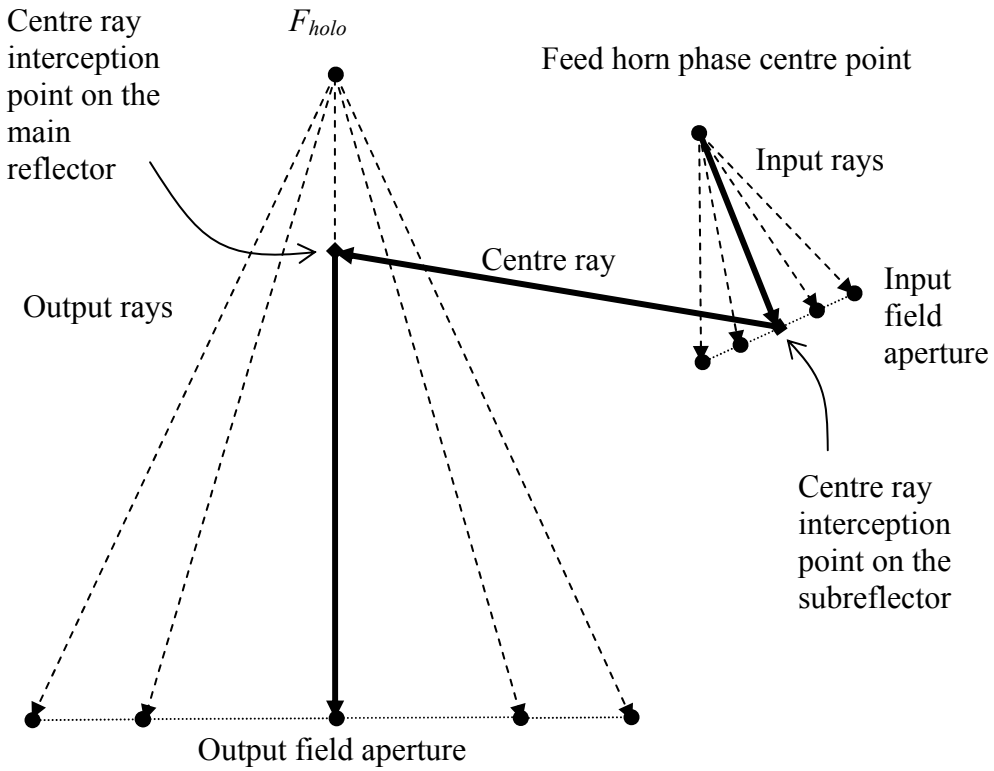

Figure 4.4 Known information in the beginning of the synthesis.

Synthesis starts from the centre ray and progress ring by ring in counter-clock wise direction to the aperture rim. First the tangential planes at the centre ray interception points are calculated using Snell's law

$$\bar{n} = \frac{\bar{s}_r - \bar{s}_i}{\left|\bar{s}_r - \bar{s}_i\right|}, \tag{4.12}$$

where $\bar{n}$ is the surface normal vector, $\bar{s}_i$ is the directional vector of the incident ray and $\bar{s}_r$ is the directional vector of the reflected ray.

After the centre ray the synthesis procedure is the same for each ray. The synthesis procedure is described in Figure 4.5. For a ray *(n,m)* the input and output rays, the anterior point *(n-1,m)* and the horizontal and vertical tangents at the anterior point are known. The subreflector point *(n,m)* is the interception point of the input ray *(n,m)* and the tangential plane at the anterior point, i.e., at the subreflector point *(n-1,m)*. The main

reflector point *(n,m)* is calculated in a similar way as the interception point of the output ray *(n,m)* and the tangential plane at the anterior point, i.e., the main reflector point *(n-1,m)*. The main reflector point is then moved along the output ray to adjust the total length of the ray *l(n,m)* from the feed horn phase centre point to the output field aperture to be same as the distance from the output field aperture point to the hologram focal point. The desired ray length is

$$l(n,m) = \sqrt{\rho'(n,m)^2 + f_{holo}^2} \,. \tag{4.13}$$

After the subreflector point and the main reflector point are known, the horizontal and vertical tangents are calculated from the input ray, the ray from the subreflector point to the main reflector point and the output ray using the Snell's law (4.12).

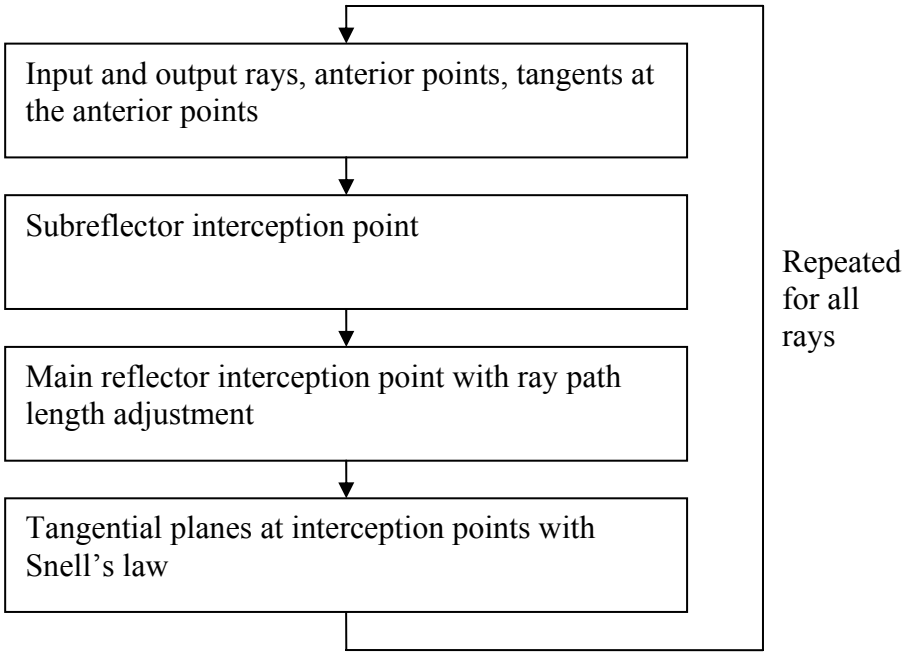

Figure 4.5 Reflector synthesis procedure.

4.3.7 Post-synthesis processing of the reflector surfaces

Planes are fitted around the shaped surfaces as the manufacturing of the reflectors require the milling profile to be known. The fitting is done with a linear extrapolation and circular rounding [Häkli 2004], [Häkli 2005c]. The orientation of the plate is computed from the rim points of the horizontal cut of the shaped surface area. The orientations of the plates, angles β_{sub} and β_{main} in Figure 4.2, and the centre ray interception points define the local reflector coordinates, i.e., the subreflector coordinates and the main reflector coordinates.

The rim of the shaped area is not exactly on a plane in the local reflector coordinates. An extrapolated linear part is added to the surface to get the rim to a plane, i.e., to the same z-coordinate in the local reflector coordinates. Circular rounding of a height h is then added to the surfaces.

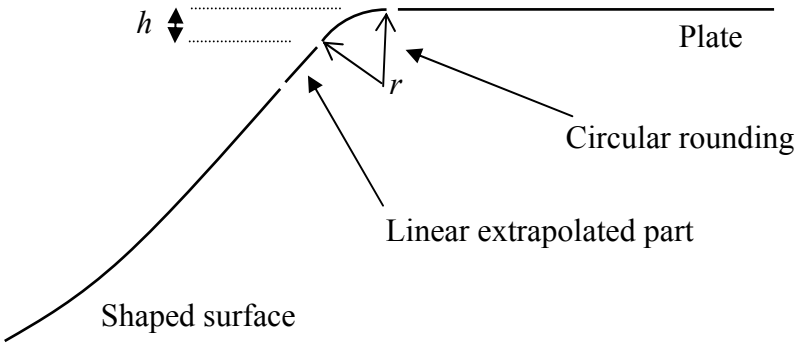

Figure 4.6 Reflector edge treatment.

4.3.8 Design example at 310 GHz

Previously, a dual reflector feed system for a hologram-based compact antenna test range has been designed. This DRFS was designed with the numerical synthesis method explained in Section 4.3 and optimised to illuminate a 600 mm hologram at 310 GHz [Häkli 2004], [Häkli 2005a], [Häkli 2005c]. The synthesis procedure was implemented as MATLAB®-programs. The DRFS was manufactured at Thomas Keating Engineering Physics, Ltd., in England.

The feed horn used is a corrugated horn with Gaussian beam. The -17.5 dB half-beam width of the horn is 20º. The desired output field was a Butterworth-type function in Equation (4.4), where ρ_c is 210 mm and N is 5. The geometrical parameters are listed in Table 4.1 and illustrated in Figure 4.1.

Table 4.1 Geometrical parameters for the 310 GHz DRFS [Häkli 2005c].

D	600 mm
D_{holo}	736 mm
f_{holo}	1800 mm
f_{sub}	100 mm
r_{sub}	150 mm
r_{main}	1550 mm
α_{feed}	270º
α_{main}	90º
θ_{feed}	21º
θ_{main}	11.55º

Edge illumination was chosen to be less than -15 dB for both reflectors [Häkli 2005c] and below -15 dB for the hologram [Häkli 2004]. 423 × 401 rays were used in the synthesis. The orientation angles of the reflector plates are β_{sub} = 43.05º and β_{main} = 44.34º. The dimensions of the subreflector are approximately 122 mm × 83 mm × 4.6 mm and 165 mm × 119 mm × 2.8 mm for the main reflector.

4.3.8.1 Simulated and measured radiation of the 310 GHz DRFS

Simulated and measured radiation of the 310 GHz dual reflector feed system is presented in [Häkli 2004] and [Häkli 2005c]. The simulations were done with GRASP8W software using physical optics (PO) and physical theory of diffraction (PTD). The measurements were done with millimetre wave vector network analyser AB Millimétre MVNA-8-350. The desired, simulated and measured horizontal and vertical beam-cuts are shown in Figures 4.7 and 4.8.

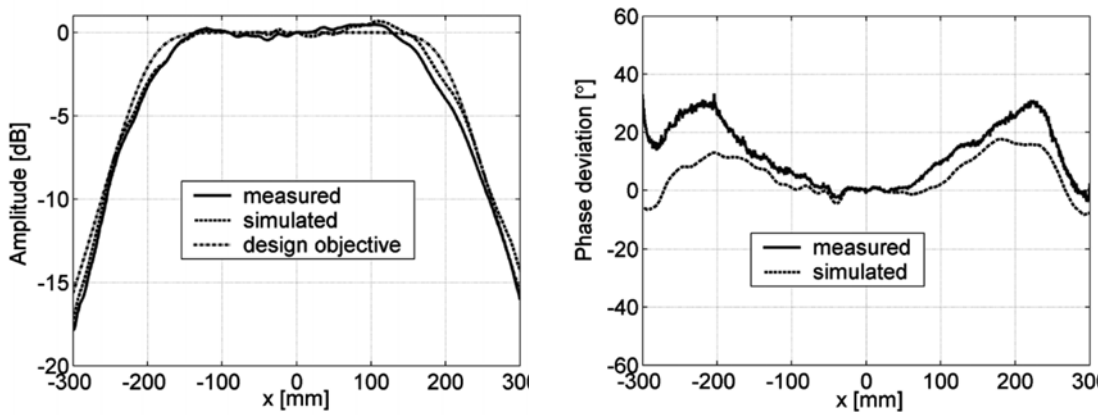

Figure 4.7 Measured and simulated amplitude and phase deviation from the spherical wave in a horizontal beam cross-cut at 310 GHz [Häkli 2005c].

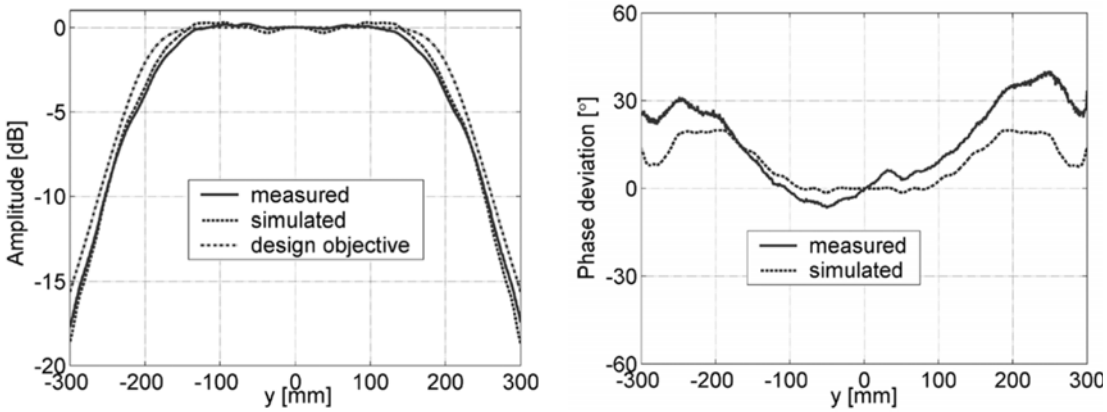

Figure 4.8 Measured and simulated amplitude and phase deviation from the spherical wave in a vertical beam cross-cut at 310 GHz [Häkli 2005c].

The measured amplitude is within 0.3 dB from the simulated amplitude and within 0.5 dB from the desired hologram illumination. The measured phase is within 30° from the ideal spherical phase within the radius of 150 mm from the centre of the beam [Häkli 2005c]. The phase deviation can be mostly compensated by placing the DRFS about 12 millimetres closer to the hologram. Cross-polarization level due to the depolarization by the DRFS is at maximum about -20 dB [Häkli 2004].

4.4 Improvements to the synthesis program

The 650 GHz dual reflector feed system was designed with the synthesis method described in Section 4.3. In the beginning of the design process it was not known how to get wider beam with a better beam quality. To study this several improvements were done to the synthesis programs. Improvements that were done include for example non-symmetric aperture mapping, reflector surface extrapolation from several known points

instead of using only one anterior point, different shapes for the reflector edge rounding and compensation of the feed horn phase error. Correction functions were added to the ray end points in the output field aperture, interception points at the subreflector and the desired ray length.

It was found that low edge illumination of the reflectors, size of the reflectors, correct choice of input and output fields and a correction function to the desired ray length affect the ripple and the shape of the output beam more than anything else. The design process of the 650 GHz DRFS is explained in Chapter 5.

5 Design of a 650 GHz dual reflector feed system

The design of the 650 GHz DRFS is described in this chapter. The DRFS was optimized for a 3.18 metre diameter hologram with f_{holo}/D_{holo} = 4. The desired hologram illumination was decided to have a -1 dB beam width corresponding to a 2 metre diameter of QZ, i.e., -1 dB beam width radius of 1190 mm in the hologram illumination. Hologram edge illumination was decided to be under -10 dB. The amplitude ripple should be less than 0.7 dB peak-to-peak and the deviation from a spherical phase originating from the hologram focal point F_{holo} should be less than 7° peak-to-peak. The maximum diameter of the shaped reflectors was decided to be approximately 200 mm to avoid problems with manufacturing accuracy. Also the size of the whole DRFS structure should be kept moderate.

In the design process the reflector surfaces were calculated with the synthesis programs described in Section 4.3. The output aperture field was simulated with the GRASP8W simulation software [Ticra] using physical optics (PO) and physical theory of diffraction (PTD). The design process is described in Section 5.1 and the simulations with GRASP8W in Section 5.1.1. In Sections 5.2-5.4, the parameters of the final design and reasons for choosing them are described. The mechanical design is presented in Section 5.5.

5.1 Design process

The iterative design process is shown in Figure 5.1. One iteration round of the design process has three parts: the synthesis of the DRFS, simulations and analysis of the results. The synthesis of the DRFS can be divided into three parts: definition of the basic geometry, definition of input and output fields and their representation with rays and the synthesis of the reflector surfaces. The field at the output aperture, i.e., the hologram illumination, is simulated using GRASP8W with physical optics (PO) and sometimes also with physical theory of diffraction (PTD). Finally the simulation results are analysed, i.e., the amplitude and the phase are calculated from the simulation results and compared to previous simulation results.

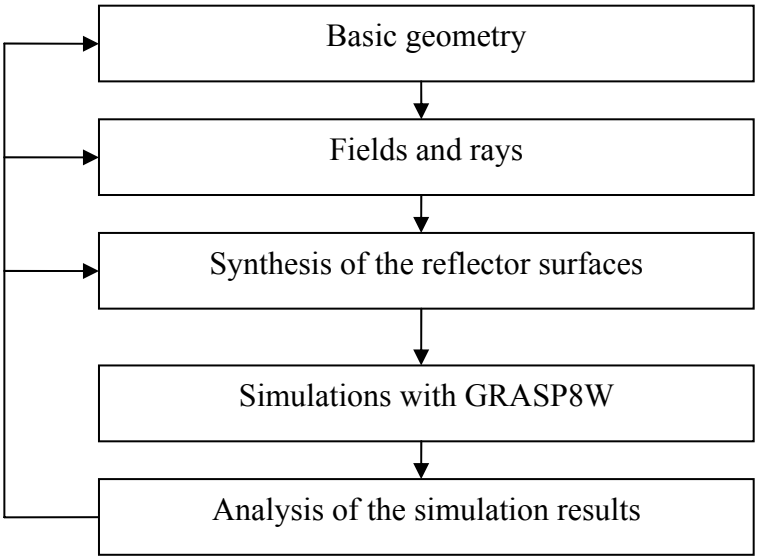

Figure 5.1 Design process.

The design process is an iterative optimization process. In general, first the parameters of the basic geometry were optimized, then the input and output fields and their representation with rays were optimized, and finally the parameters of the reflector synthesis were optimized. Each of those three steps are discussed separately in more detail in Sections 5.2-5.4. In practice the design process is not that straightforward because all of the steps in the design process affect each other.

Each parameter was optimized by synthesizing the surfaces with a number of different values for the parameter. Then the synthesized surfaces were simulated and the results analysed. The best value for the parameter, based on the simulation results, was used when the next parameters were optimized. In this way it was possible to study separately how each parameter affected the radiation of the DRFS.

In the beginning of the 650 GHz DRFS design it was not known if the desired hologram illumination is realizable or not. The design process was repeated many times to find the realizable beam width with desired beam quality and to find out how to decrease the ripple and how to correct the shape of the output beam, i.e., the synthesis errors. The design process, described in Figure 5.1, has to be repeated for each beam width of the desired output field and then the ripple must be minimised.

5.1.1 Simulations with GRASP8W

The simulations were done with GRASP8W software by Ticra Engineering Consultants [Ticra] using physical optics (PO) and sometimes also physical theory of diffraction (PTD). In GRASP8W the surface currents are calculated at a regular polar grid using the physical optics (PO) from the incident field. The reflected field is calculated from the surface currents. The physical theory of diffraction is used to calculate the reflector edge currents. The surface currents are usually called the PO currents and the edge currents are called the PTD currents. The feed horn model is presented in Section 5.1.1.1 and the *PO Convergence* object of the GRASP8W software that was used to determine the number of current elements is presented in Section 5.1.1.2.

The effect of the PTD currents to the output aperture field was very small when the edge illuminations of the reflectors were small. Typically, the maximum difference between simulation results with and without the PTD was less than 0.02 dB and 0.2° in the horizontal and vertical cuts. The simulation results given in this chapter and in Chapter 6 were calculated without the PTD currents, unless separately mentioned. The computation time of simulations with the PO currents was only a fraction of the time needed for simulations with both PO and PTD.

The reflector surface data were defined in a regular *xy*-grid, with $\Delta x = \Delta y = 0.5$ mm. Data for the regular *xy*-grids were interpolated from the synthesized surfaces that were defined at irregular grids at the reflection points of the rays. The reflector rims were defined as ellipses. Only the surface data points inside the rim ellipses were used in the simulations. Cubic interpolation is used in GRASP8W to calculate the surfaces at the points where the currents are calculated. Large number of points was used to ensure good accuracy of the surface points despite these two interpolations. $\Delta x = \Delta y = 0.5$ mm was found to be enough for the regular *xy*-grids as there was practically no difference between the simulation results of $\Delta x = \Delta y = 0.1$ mm grid and $\Delta x = \Delta y = 0.5$ mm grid.

Computation time was significantly reduced compared to what was needed for the 310 GHz DRFS [Häkli 2004]. In that version of the GRASP that was then available, the reflector surfaces had to be originally defined for the GRASP in an irregular grid and interpolated with quintic pseudosplines (QPS). The QPS interpolation is computationally

heavy. Using the much faster cubic interpolation from the regular *xy*-grid and not calculating the PTD currents every time reduced the computation time significantly. The reduction in computation time allowed more simulations to be done.

5.1.1.1 Feed horn model

The simulated radiation pattern of the 650 GHz corrugated feed horn was used in the simulations. The radiation pattern was provided by the feed horn manufacturer, Thomas Keating Ltd., as amplitude and phase at the vertical polarization in horizontal, diagonal and vertical cuts. The amplitude and phase of the cross-polarization was defined only in the diagonal cut. The radiation pattern is defined with 0.3° spacing in the θ-direction from 0° to 54°. The feed horn pattern cuts at the vertical polarization are shown in Figure 5.2.

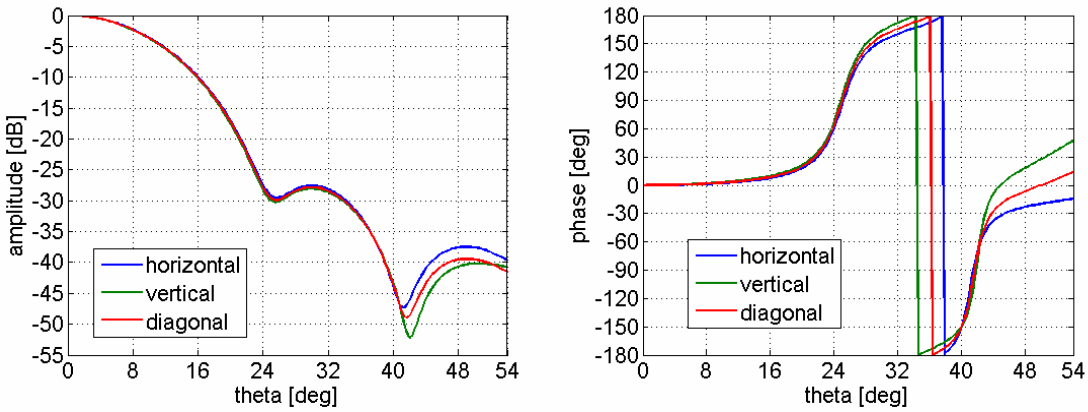

Figure 5.2 Amplitude and phase of the horizontal, vertical and diagonal cuts of the feed horn radiation pattern at the vertical polarization.

In GRASP8W, the radiation pattern in direction (ϕ,θ) is interpolated from the field cuts. The field data is converted to azimuthal modes, i.e. Fourier coefficients are determined, for each θ-value. The field at the ϕ-value is calculated from these azimuthal modes. The interpolation in the θ-direction is done as a third order polynomial interpolation [Pontoppidan 2003]. The field calculated in this way is the far-field E_{far}. The field at distance r from the phase centre point is determined from [Pontoppidan 2003]:

$$E(r) = E_{far}\frac{e^{-jkr}}{kr}, \tag{5.1}$$

where k is the wave number and r is the distance to the phase centre point.

The feed horn model is a far-field model and it does not model the near-field effects. This is not a problem because the subreflector is in the far field of the feed horn as the far-field criterion from (2.1) is only 17 mm for the about 2 mm diameter feed horn at 650 GHz.

5.1.1.2 Number of current elements

The number of current elements has to be large enough for the physical optics (PO) and the physical theory of diffraction (PTD) to give accurate results. In GRASP8W, the number of current elements is defined by two variables: *po1* in θ-direction and *po2* in ϕ-direction. The number of PTD current elements is usually same as *po2*. The number of current elements can be set by the user or calculated automatically with the *PO Convergence* object of the GRASP8W. The required number of the current elements depends on the size and the shape of the reflector compared to the wavelength, the desired field accuracy and the beam angle in which the computed field should converge.

The *PO Convergence* object calculates the required number of current elements as the function of the desired field accuracy defined by the user. The values for the variables *po1* and *po2* for all of the reflectors are varied independently until the desired field accuracy compared to the peak value is achieved in all of the field points defined by the user. The *PO Convergence* object also calculates and saves the currents, so it is not necessary to re-calculate them after the *PO Convergence*. The field accuracy *F[dB]* ($F < 0$) to be used in the *PO Convergence* can be estimated from [Jensen 2003]:

$$F[dB] \approx -Y[dB] - 20dB + 20\log(X[dB]), \tag{5.2}$$

where *Y[dB]* is the field level below the peak ($Y > 0$) where the maximum error is ± *X[dB]*. Some examples of maximum error as function of the desired field accuracy are presented in Table 5.1.

Table 5.1 Examples of maximum error as function of field accuracy.

field accuracy *F[dB]*	*Y[dB]* below peak	maximum error ± *X[dB]*
-60	10	0.03
-60	20	0.1
-90	20	0.003
-90	60	0.3

In the design process shown in Figure 5.1, the simulations were usually done so that first the *PO Convergence* was used to calculate the currents and then the field at the hologram

was calculated. The field accuracy F = -60 dB is enough to determine the required number of current elements. Only 9 field points were used in the *PO Convergence* as it is enough to include points from the centre of the beam, i.e. the peak value, and the outermost point of the area where the field accuracy should be achieved. The *PO Convergence* was repeated every time the size of the reflectors changed. The number of current elements determined with *PO Convergence* with field accuracy F = -90 dB was used for all of the final simulation results presented in Chapter 6.

5.2 Basic geometry

The basic geometry of the designed 650 GHz DRFS is illustrated in Figure 5.3. The figure is not in scale.

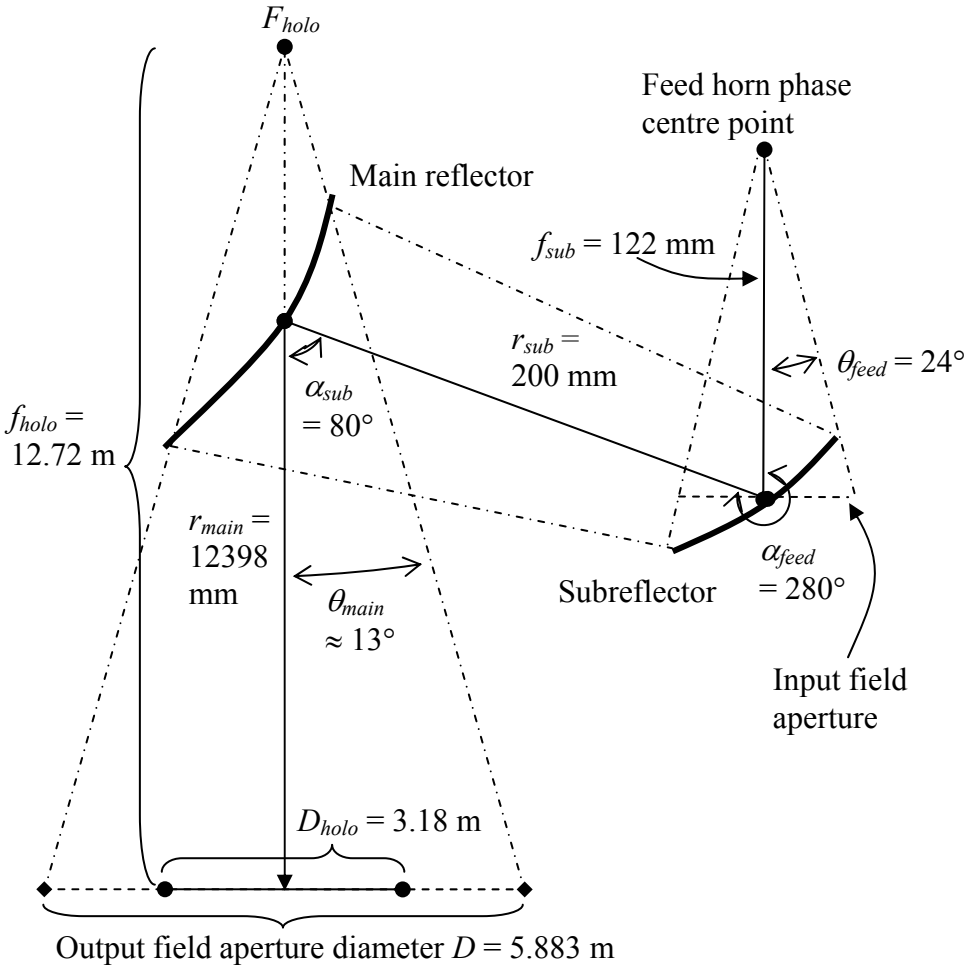

Figure 5.3 Basic geometry of the 650 GHz DRFS.

The edge illuminations of the reflectors have to be low. The output field aperture diameter D is chosen to be much larger than the hologram diameter D_{holo} to get the main

reflector edge illumination much lower than the hologram edge illumination. The incident field on the main reflector, shown in Figure 5.6, and thus also the main reflector edge illumination are mainly determined from the desired output field, shown on Figure 5.4 b), as the subreflector is mainly responsible for modifying the amplitude. The feed angle θ_{feed} and feed horn beam width determine the subreflector edge illumination. Low edge illumination reduces the edge diffraction, which is one of the main sources of ripple.

The reflector angles α_{feed} and α_{sub} are 80° and 280°, instead of 90° and 270° as in the 310 GHz DRFS [Häkli 2005a], [Häkli 2004], to keep the structure compact and reflector sizes reasonable even though f_{sub} and r_{sub} are increased. This also decreases the maximum cross-polarization level by about 1.5 dB according to the simulations.

The reflector sizes are mainly determined by the basic geometry: the subreflector size by f_{sub}, θ_{feed} and α_{feed} and the main reflector size by r_{main}, D and α_{sub}. Also the choice of the input and output fields affect the sizes of the reflectors. It was discovered that the size of the reflectors should be as large as possible. With the basic geometry parameter values in Figure 5.3 the maximum reflector diameter, the main reflector width, is about 200 mm.

5.3 Input and output fields and rays

The input field is the simulated radiation field of the corrugated feed horn. The feed horn has a Gaussian beam and the -30 dB half-beam width is 25°. Horizontal, vertical and diagonal cuts of the feed horn radiation pattern are shown in Figure 5.2. The input field at the input field aperture, shown in Figure 5.4 a), is interpolated from the feed horn radiation pattern. The phase of the feed horn is not included in the synthesis of the reflector surfaces but it is included in the feed horn model used in the GRASP simulations.

The desired output field is the output field defined in the synthesis program before the synthesis of the reflector surfaces. The desired output field has -1 dB beam radius 1272 mm (80% of the hologram radius 1590 mm) and hologram edge illumination -15 dB. The desired output field is rotationally symmetric before the rotationally symmetric mapping described in Section 4.3.5. The desired output field was chosen based on the desired -1 dB beam width and the desired hologram edge illumination. The

shape of the output field outside the hologram, i.e., $\rho > 1590$ mm, affects the shape of the reflectors near the edges. The reflector edges affect edge diffraction and size of the reflectors, so the desired output field has to be optimized also outside the hologram area.

The desired output field before the mapping, shown in Figure 5.4 b), is a rotationally Butterworth-type function as shown Equation (4.4), where $\rho_c \approx 1355$ mm and $N = 10.7$, when $\rho < 1590$ mm. The desired output field after the mapping, shown in Figure 5.4 c), is calculated from the input ray tube powers and the output ray grid. The fields in Figure 5.4 are defined in the aperture field ray grids, where $\Delta\phi = 0.6°$ and $\Delta\rho$ is shown in Figure 5.5.

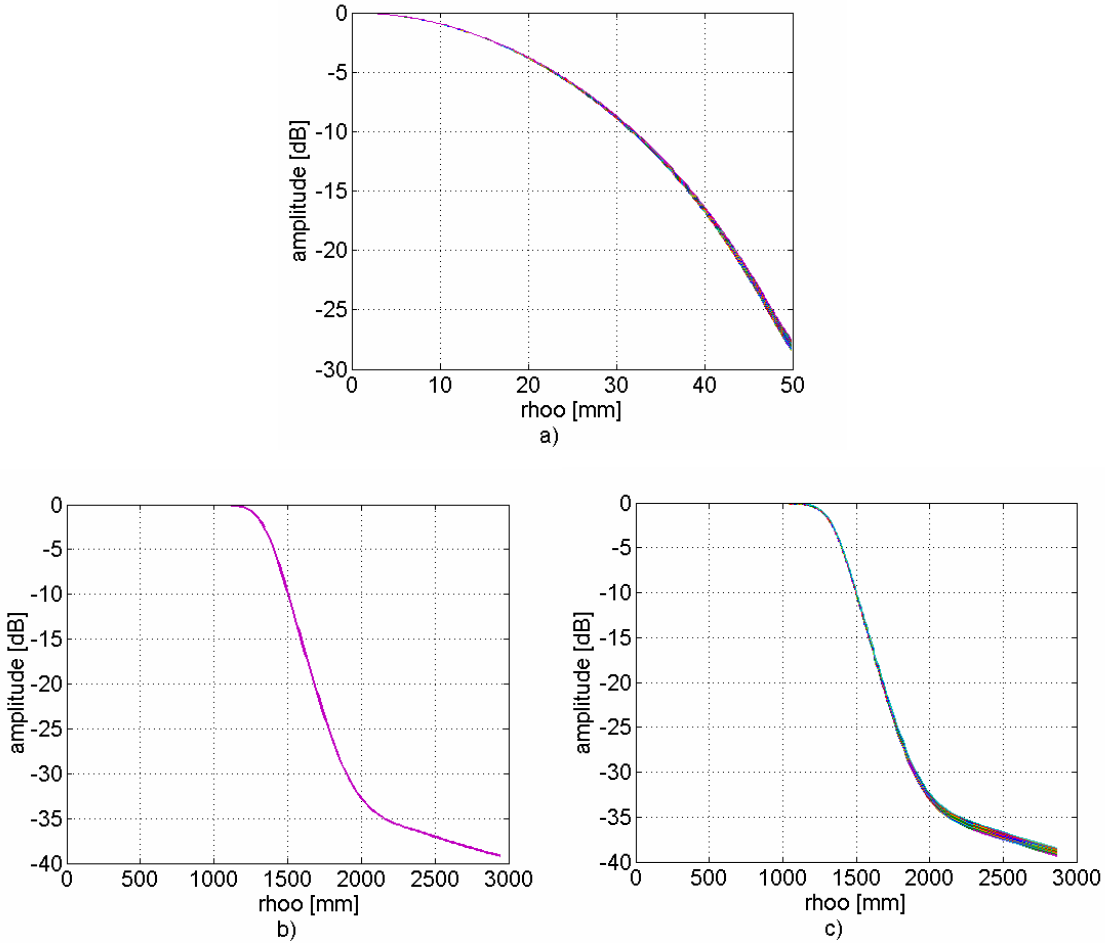

Figure 5.4 Input and output field amplitudes: a) Input field in the input field aperture, b) desired output field in the output field aperture, and c) desired output field after the rotationally symmetric aperture mapping.

The desired output field beam has to be chosen to be wider and the hologram edge illumination of the desired output field to be lower than for the desired hologram illumination. The difference between the desired output field and the simulated output

aperture field is larger if a wider beam is attempted and smaller if a narrower beam is attempted.

The ratio of the input and output field beam widths (and shapes) has to be right. For a given output beam there is an optimum beam width of the input field. The optimum beam width of the input field was found to be the same as the beam width of the feed horn of the 310 GHz DRFS.

5.3.1 Ray grids

The rays are determined from the fields as described in Section 4.3. 601 × 601 rays were used. The output ray grid is calculated with the rotationally symmetric aperture mapping described in Section 4.3.5. In the aperture mapping the fields are assumed to be rotationally symmetric. This causes the so-called mapping error. This mapping error causes the desired output beam to be wider in horizontal cut than in the vertical cut after the aperture mapping. The output field after aperture mapping is shown in Figure 5.4 c). The mapping error, i.e., the difference between Figures 5.4 b) and c), is small and can be neglected.

In the 310 GHz DRFS, the input ray grid was defined as constant angular and radial polar grid and 423 × 401 rays were used [Häkli 2005a], [Häkli 2004]. For the 650 GHz DRFS the number of rays was increased and the input ray grid changed because the distance between rays, i.e., the distance between the surface data points, towards the edge of the main reflector grew very large. If the distance between the surface data points is too large the shape of the reflector is defined by interpolations instead of the synthesis. The ray density was increased towards the edge of the input field aperture. $\Delta\rho$ of the input ray grid is shown in Figure 5.5 a) and $\Delta\rho'$ of the output ray grid in Figure 5.5 b). With the maximum $\Delta\rho'$ of the output ray grid of about 47 mm the maximum distance between the synthesized surface data points is only a few millimetres.

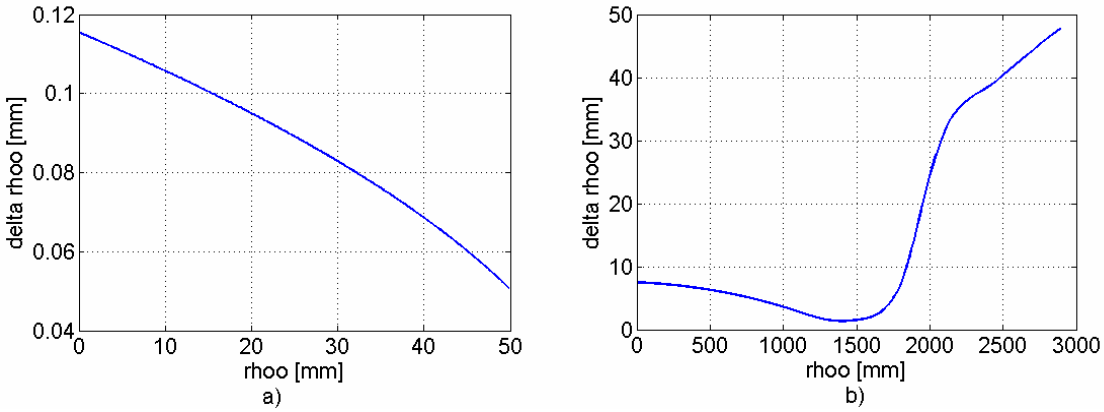

Figure 5.5 Ray spacing in the radial direction: a) $\Delta\rho$ of the input ray grid, b) $\Delta\rho$' of the output ray grid.

5.3.2 Multiple reflections and direct radiation from the feed horn

The simulations with GRASP8W simulate the reflectors separately; first the currents on the subreflector are calculated from the feed horn radiation pattern, then the currents on the main reflector are calculated from the subreflector currents, and finally the output aperture field is calculated from the main reflector currents. The possibility of multiple reflections and direct radiation from the feed horn to the hologram has to be studied separately. Multiple reflections can be studied by calculating how much of the power goes to the reflectors.

The possibility of direct radiation from the feed horn to the hologram can be ruled out by studying the basic geometry in Figure 5.3. Because the dimensions of the DRFS are small compared to the distance to the hologram and because the feed angle θ_{feed} is larger than θ_{main}, the subreflector blocks the radiation from the feed horn to the output field aperture. Therefore, direct radiation from the feed horn to the hologram is not possible.

The subreflector illumination is defined by the feed horn radiation pattern and the feed angle θ_{feed}. The input field at the input field aperture, i.e., the field illuminating the subreflector, is shown in Figure 5.4 a). The subreflector edge illumination is about -27.5 dB. The maximum field level outside the subreflector is about the same as the subreflector edge illumination.

The simulated total power on the main reflector surface is shown in Figure 5.6. The total power is the sum of the *x*-, *y*- and *z*-polarizations in the plane in which the main reflector surface data are defined. The field was calculated in a polar grid at points that are inside the rim ellipse defined for the main reflector. From Figure 5.6 it can be seen that the main reflector edge illumination is at maximum about -37 dB compared to the maximum.

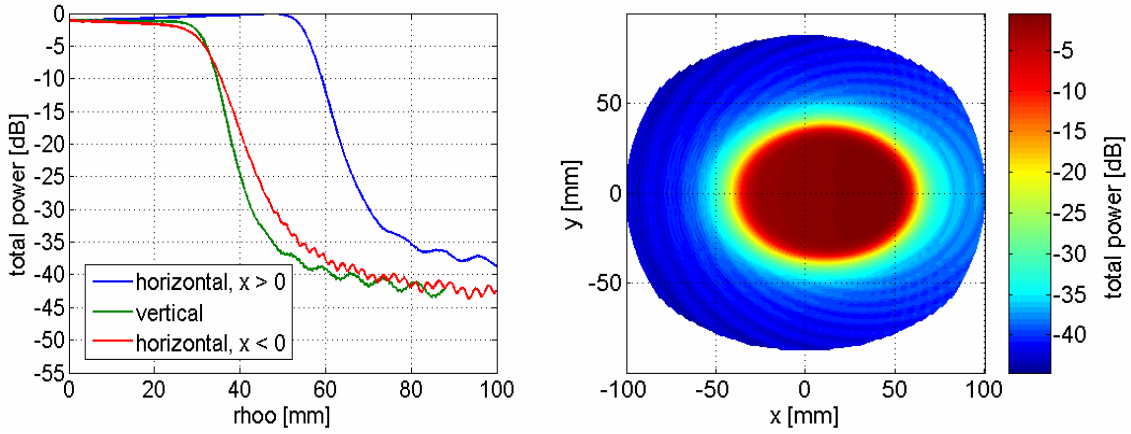

Figure 5.6 Simulated total power on the surface of the main reflector.

The illumination from the main reflector to the subreflector was studied by simulating the total power in the horizontal cut of the output aperture. The simulated total power is shown in Figure 5.7 as the function of θ–coordinate of the global coordinates, which have the origin at the hologram focal point F_{holo} and the *z*-axis towards the hologram centre. The hologram edge is at $\theta \approx 7.1°$, the edge of the output field aperture is at $\theta_{main} \approx 13.0°$ and the subreflector edge closest to the output beam centre is at $\theta \approx 15.7°$. The illumination from the main reflector to the subreflector is at maximum about -55 dB.

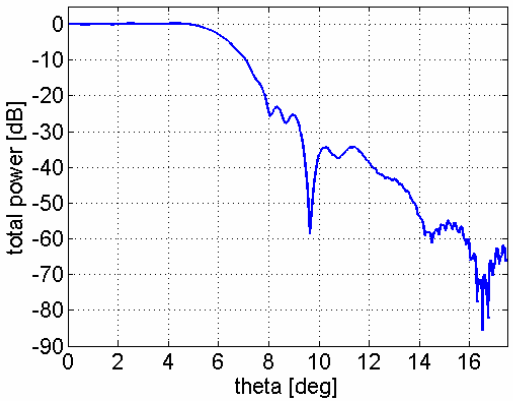

Figure 5.7 Simulated total power of the horizontal cut, x > 0, in the output aperture.

5.4 Synthesis of the reflector surfaces

In the synthesis of the reflector surfaces the synthesis program described in Section 4.3.6 was used with a correction function to the desired ray length calculated from Equation (4.6). Using the correction function corresponds to optimizing the phase of the desired output field, i.e., the phase of the output field defined in the synthesis. In the synthesis of the reflector surfaces the ray length is adjusted by moving the main reflector point, which then affects the tangential planes and the shape of the both reflectors. Therefore, by changing the phase of the desired output field it is possible to change the shape of the amplitude and the phase of the output aperture field.

Figure 5.8 (and Figures 4.5 and 4.6) shows an example of simulated amplitude and phase deviation before the optimization of the phase of the desired output field.

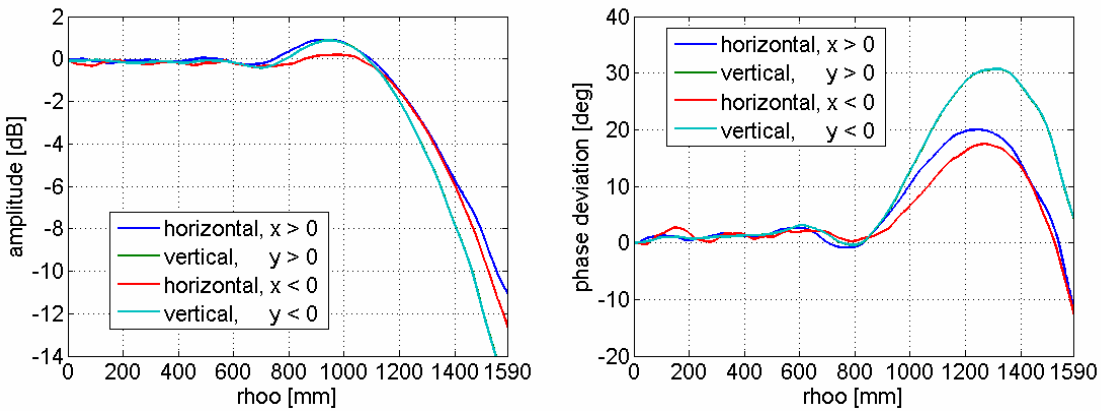

Figure 5.8 An example of simulated amplitude and phase deviation in the output aperture field cuts before the optimization of the output field phase.

There is a shoulder in the amplitude where the desired output field changes rapidly and the beam is clearly narrower in the vertical direction than in the horizontal direction. These errors are corrected by optimizing the desired output field phase in the synthesis. The phase deviation from the spherical wave of the desired output field in the synthesis is shown in Figure 5.9 in the output field aperture. The negative phase deviation of the desired output field increases the desired ray lengths. The maximum of about 70° corresponds to 90 μm longer rays.

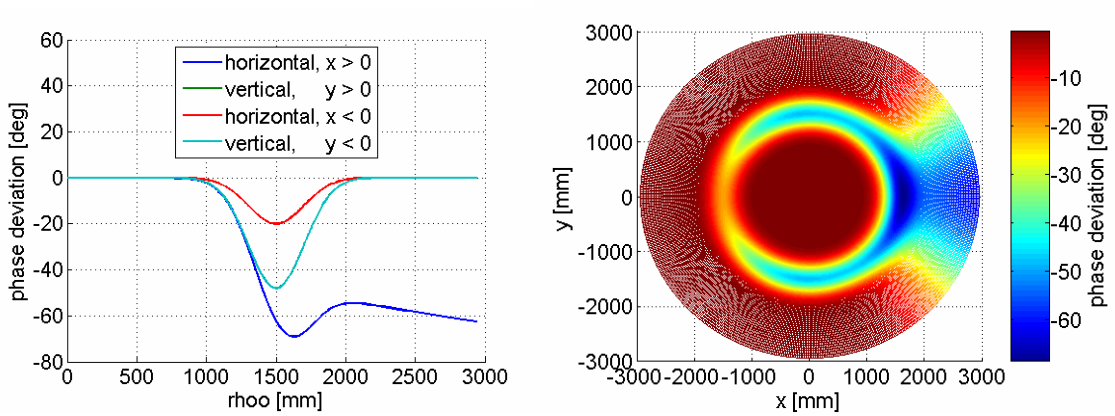

Figure 5.9 Phase deviation from the spherical wave of the desired output field in the output field aperture.

The optimization can be done separately for each of the radial cuts. The vertical cuts and the horizontal cut where $x < 0$, have been optimized only to reduce the shoulder in the amplitude. Removing the shoulder increases the hologram edge illumination. In the horizontal cut where $x > 0$ it was necessary to decrease the hologram illumination by decreasing the phase of the desired output field as shown in Figure 5.9. Removing the shoulder in the amplitude also reduces the phase deviation from the spherical wave of the output aperture field.

5.4.1 Edge rounding

Different sizes of circular and elliptical rounding to the reflector edges were studied. Because of the low reflector edge illuminations different shapes and sizes of the edge rounding affect only the shape, but not the size, of the ripples in the simulated output aperture field. For the final design of the 650 GHz DRFS, a circular rounding of height $3 \cdot \lambda/4$ in the subreflector and $\lambda/4$ in the main reflector was used. A circular rounding is illustrated in Figure 4.6.

5.4.2 Reflector surfaces

The dimensions of the reflectors of the designed 650 GHz DRFS are 146 mm × 109 mm × 7.0 mm (width × height × depth) for the concave subreflector and 203 mm × 160 mm × 4.4 mm for the convex main reflector. The reflector surfaces are shown in Figure 5.10, where the reflectors are defined in the subreflector and main reflector coordinates described in Section 4.3.1.1. The subreflector and main reflector coordinate angles are

$\beta_{sub} \approx 37.61°$ and $\beta_{main} \approx 39.23°$, respectively. The horizontal cuts of the reflector surfaces are shown in Figure 5.11.

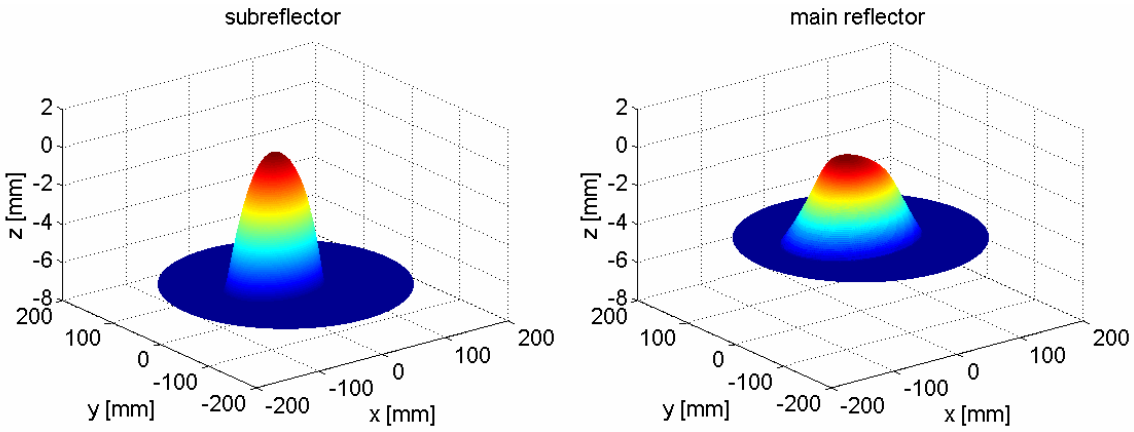

Figure 5.10 Reflector surfaces.

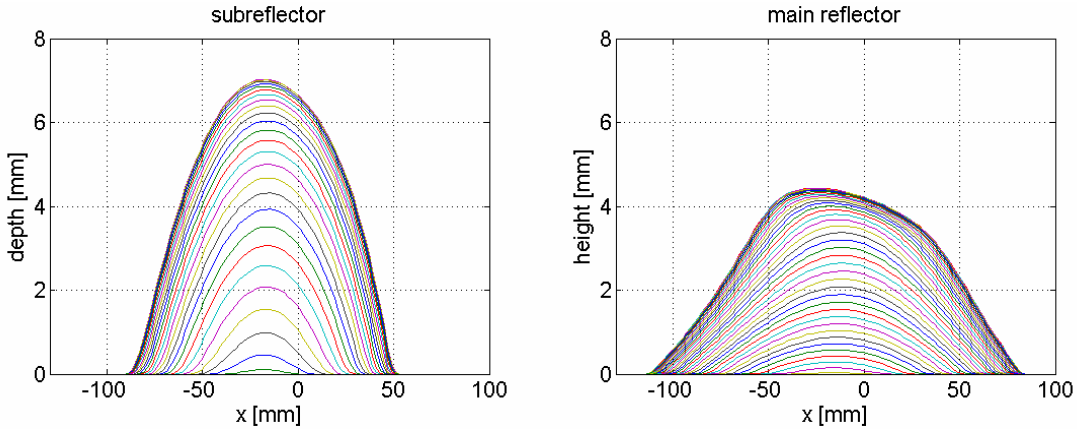

Figure 5.11 Horizontal cuts of the reflector surfaces.

5.5 Mechanical design

The 650 GHz DRFS is manufactured in England at Thomas Keating Engineering Physics, Ltd., as an integrated quasi-optical system. The surface data for the manufacturing were defined as the *z*-values in 99 × 99 points at the *xy*-planes of the subreflector and main reflector coordinate systems. The surface data for the milling machine are computed with meshing software, which generates NURBS (non-uniform rational B-spline) surfaces. The NURBS surfaces will give a good fit to the given surface data despite the relatively small number of data points.

The reflectors are cut along elliptical rims. The rim ellipse parameters; the horizontal half-axis *a*, the vertical half-axis *b* and the ellipse centre in the reflector coordinates, are presented in Table 5.2.

Table 5.2 Rim ellipses.

Reflector:	*a* [mm]	*b* [mm]	centre [mm]
Subreflector	75.4	67.4	(-18.528 , 0)
Main reflector	102.9	82.8	(-14.773 , 0)

The feed horn is held in place with a horn clamp. The 650 GHz feed horn positioning is illustrated in Figure 5.12. A hole is added to the feed horn flange and to the RAM plate to ensure precise feed horn orientation and polarization. A precise spacer between the horn flange and the RAM plate is designed so that the phase centre point of the 310 GHz feed horn is positioned correctly, i.e., to the same point as the phase centre point of the 650 GHz feed horn.

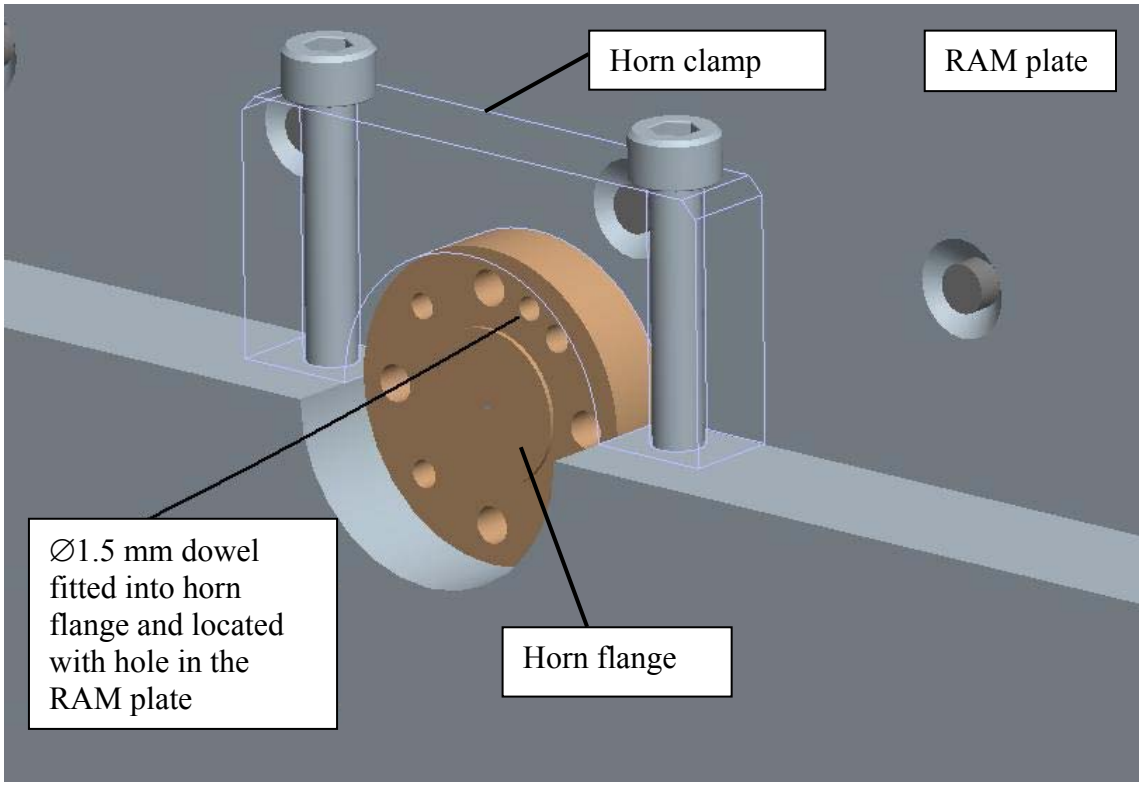

Figure 5.12 The 650 GHz field horn positioning.

Figure 5.13 shows a 3-D model of the DRFS structure. The dimensions of the 650 GHz DRFS are approximately 400 mm × 210 mm × 270 mm, not including the 140 mm × 220 mm area reserved for the transmitter behind the feed horn. All the internal walls

around the reflectors and the feed horn, the floor, and the ceiling inside the DRFS structure are coated with radar absorbing material (RAM). Vertical and horizontal reference planes will be needed to align the DRFS. The rear and front views of the designed DRFS structure are shown in Figure 5.14.

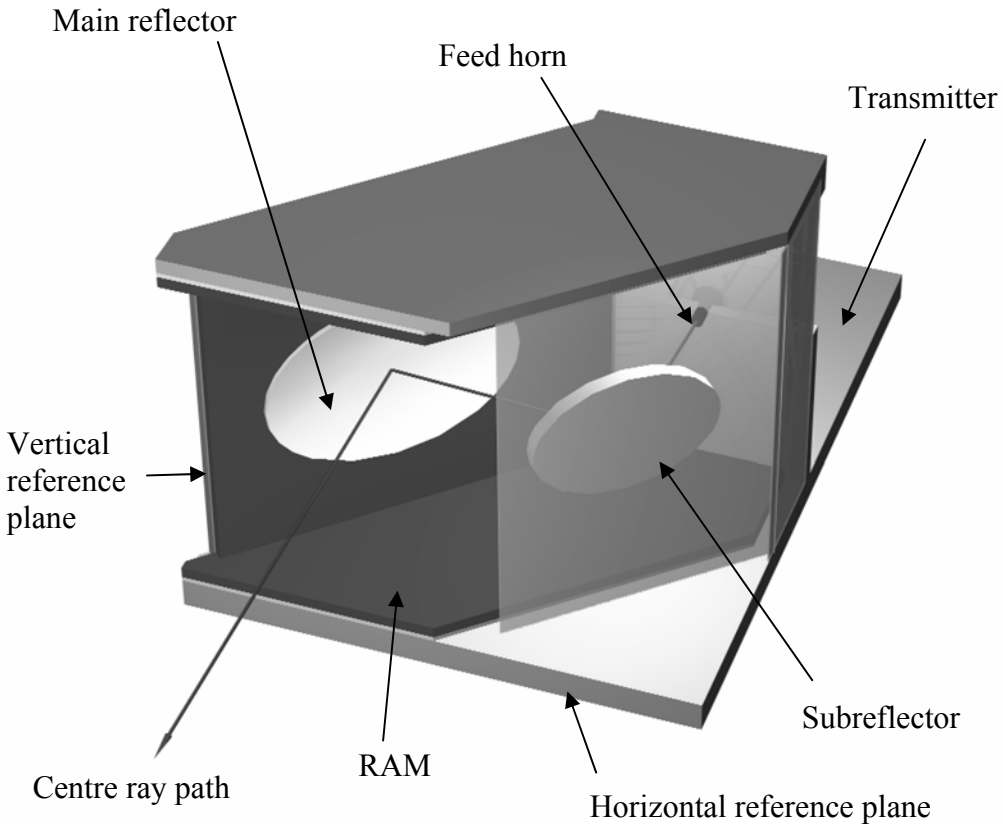

Figure 5.13 3-D model of the DRFS structure.

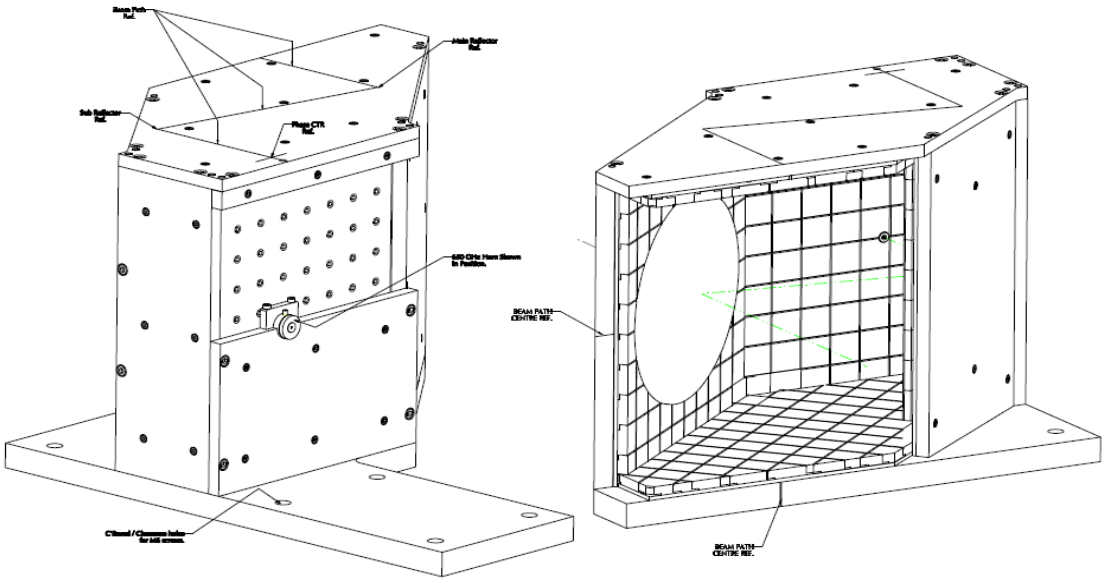

Figure 5.14 Rear and front views of the DRFS structure.

6 Simulation results

The simulation results of the final design of the 650 GHz dual reflector feed system (DRFS) are presented in this chapter. The simulations were done with GRASP8W, as explained in Section 5.1.1. The simulated amplitude and phase deviation of the hologram illumination at the vertical polarization are presented in Section 6.1 and the cross-polarization results are presented in Section 6.2. The beam propagation, i.e., how the output field of the DRFS changes as the function of the distance from the hologram focal point F_{holo}, is presented in Section 6.3. The effect of the distance from the DRFS to the hologram is studied in Section 6.4. One of the advantages of using a modified illumination of the hologram is that the hologram can be designed to operate at both the vertical and the horizontal polarizations. The simulation results at the horizontal polarization are presented in Section 6.5. Accurate measurements at the 650 GHz may not be possible, therefore the 650 GHz DRFS will be measured also at 310 GHz. The simulation results using the existing 310 GHz feed horn is presented in Section 6.6.

6.1 Amplitude and phase

The simulated amplitude and phase deviation of the 650 GHz DRFS are presented in this section. The simulation results, shown in Figure 6.1, were calculated using both physical optics (PO) and physical theory of diffraction (PTD). The phase deviation is the difference between the simulated phase and the phase of a spherical wave-front originating from the hologram focal point F_{holo}. The -1 dB beam area of the simulated amplitude and phase deviation are shown in Figure 6.2.

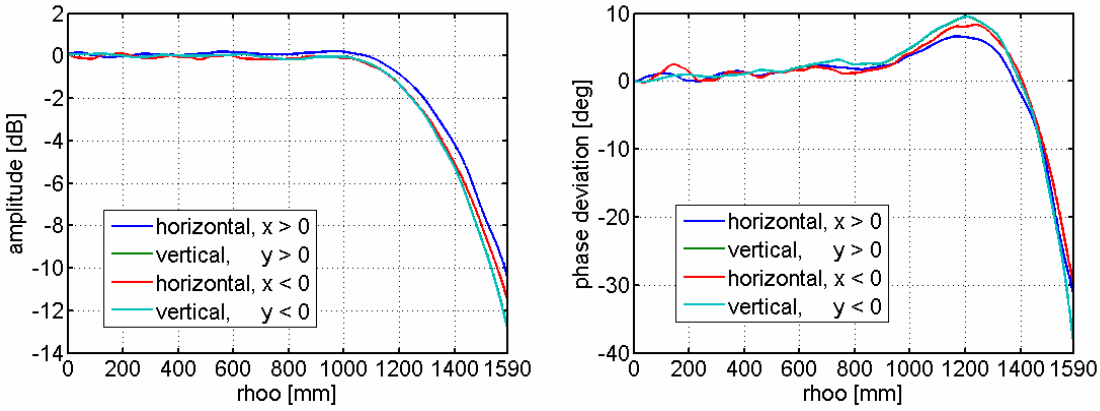

Figure 6.1 Simulated amplitude and phase deviation of the 650 GHz DRFS.

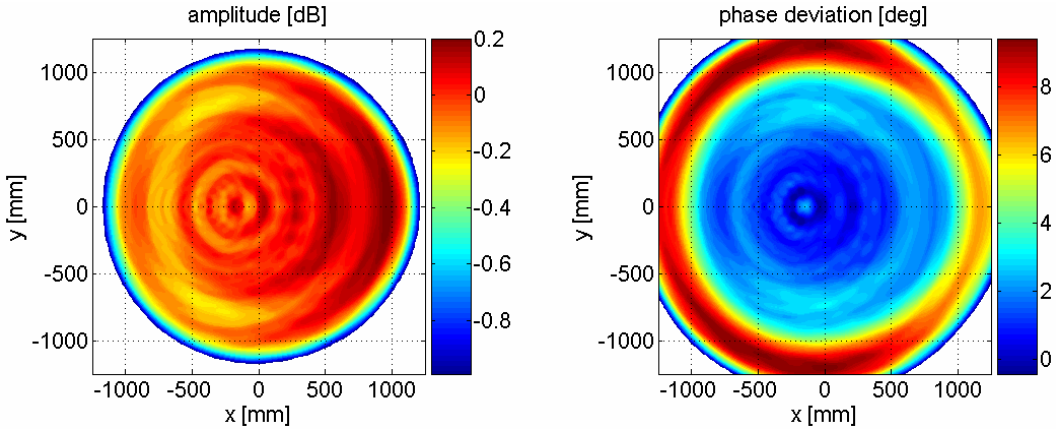

Figure 6.2 Simulated amplitude and phase deviations in the -1 dB beam area.

The -1 dB beam radius is about 1170 mm (74% of the hologram radius) and the hologram edge illumination is less than -10 dB. The amplitude ripple in the -1 dB beam area is 0.45 dB peak-to-peak (0.24 dB rms) and the phase deviation is 5° peak-to-peak (0.8° rms).

The 3.18 metre diameter hologram for the hologram-based compact antenna test range at 650 GHz, presented in Section 2.3, is designed for a rotationally symmetric Butterworth-type illumination function in Equation (4.4), where $N = 6$ and $\rho_c = 1310$ mm. The phase of the illuminating field is assumed to be an ideal spherical wave phase front originating from the hologram focal point. The parameters N and ρ_c were chosen based on the simulation results of the 650 GHz DRFS.

6.2 Cross-polarization

The cross-polarization of the DRFS is relatively high, in the -1 dB beam area at maximum -18 dB and near the hologram edges up to -15 dB in the vertical cut. The cross-polarization level of the feed horn does not affect the cross-polarization of the DRFS, because the cross-polarization is dominated by the depolarization, i.e., the part of the power that couples from the vertical to the horizontal polarization in the reflections. Depolarization is caused by the offset structure of the feed system and the shaped surfaces of the reflectors. Cross-polarization is not taken into account in the synthesis. A possibility of using a polarization grid in front of the DRFS will be studied later. Simulated cross-polarization level at the vertical polarization is shown in Figure 6.3.

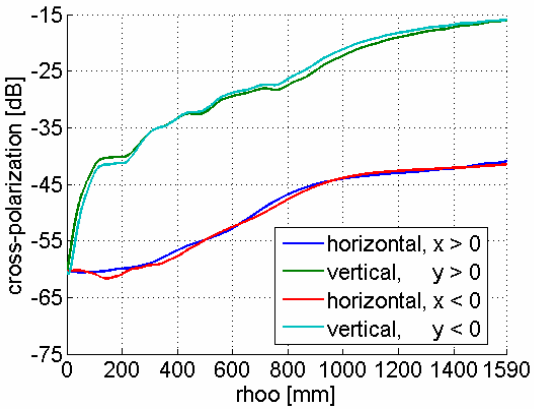

Figure 6.3 Simulated cross-polarization level at 650 GHz.

6.3 Beam propagation

The DRFS has been simulated for a 0.6 metre and a 5 metre hologram, i.e., at 2.1 metre and 20 metre distances from the focal point F_{holo}. The simulations show that the beam width and the quality of the beam do not depend on the distance from the DRFS. The 650 GHz DRFS can be used to illuminate a hologram of any size that has $f_{holo}/D_{holo} = 4$. The simulation results are presented in Figures 6.4 and 6.5.

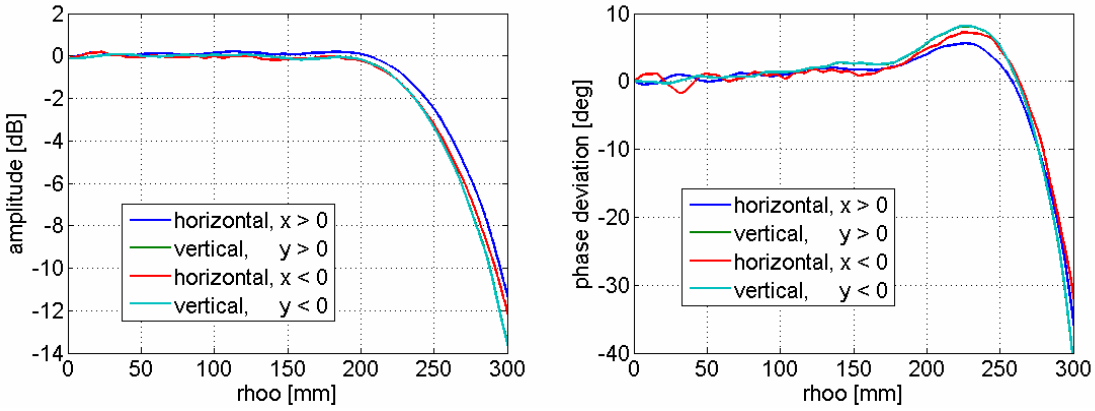

Figure 6.4 Simulated amplitude and phase deviation of the illumination for a 0.6 metre diameter hologram.

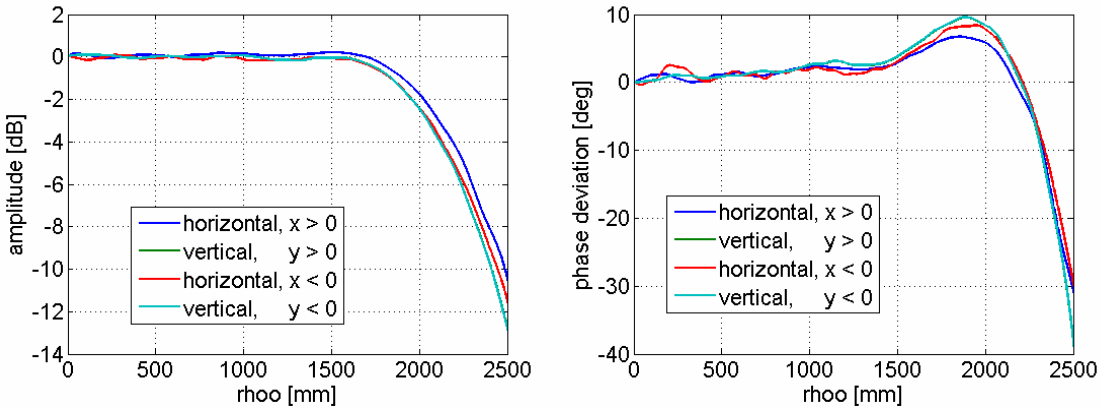

Figure 6.5 Simulated amplitude and phase deviation of the illumination for a 5 metre diameter hologram.

6.4 Distance to the hologram

The quiet-zone is optimized by finding the optimum place for the DRFS. The phase deviation, shown in Figures 6.1 and 6.2, can be mostly compensated in the -1 dB beam area by placing the DRFS two millimetres closer to the hologram. This about two millimetre difference can be considered to be a synthesis error, i.e., it can be considered as the difference in location of the focal point of the DRFS, F_{holo} in Figure 5.3, compared to the hologram focal point.

The Figure 6.6 shows the phase deviation at distances r = 12718 mm (f_{holo} – 2 mm) and r = 12720 mm (f_{holo}) from the origin of the global coordinates (F_{holo} in Figure 5.3). In both cases the phase deviation is the simulated phase compared to the phase of the spherical wave originating f_{holo} = 12720 mm from the hologram centre, i.e., originating from the hologram focal point. The difference in simulated amplitudes and cross-polarizations is small.

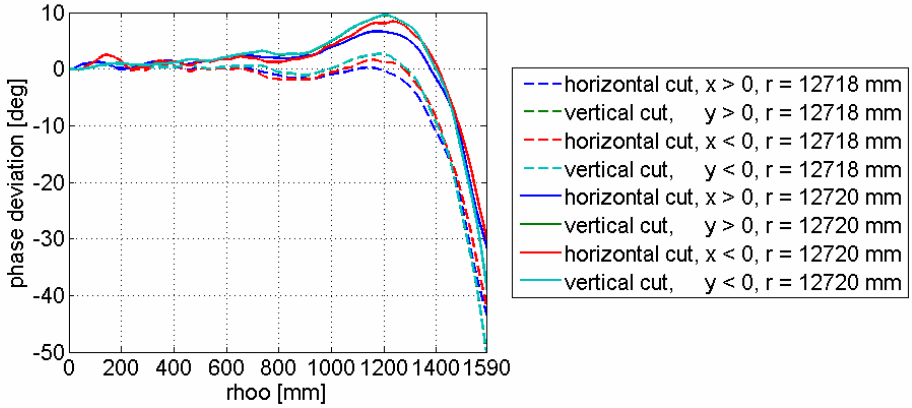

Figure 6.6. The simulated phase deviation at r = 12718 mm and r = 12720 mm.

6.5 Horizontal polarization

The 650 GHz DRFS can be used also at the horizontal polarization by rotating the 650 GHz feed horn by 90°. Because the amplitude tapering is done in the hologram illumination, the narrow slots can be avoided in the hologram pattern and the hologram can be optimized also for the horizontal polarization.

The simulation results at the horizontal polarization at 650 GHz are shown in Figure 6.7. The differences between the vertical polarization, in Figure 6.1, and the horizontal polarization, in Figure 6.7, are caused by the asymmetry of the feed horn radiation pattern. After the feed horn is rotated 90°, the feed horn radiation pattern is slightly wider in the vertical cut than in the horizontal cut, instead of being wider in the horizontal cut as in the vertical polarization. This makes the DRFS beam wider in the vertical cut and narrower in the horizontal cut. The beam width, the amplitude ripples, the ripples in the phase deviation, the hologram edge illumination and the cross-polarization are practically equal in the simulation results of the both vertical and horizontal polarizations.

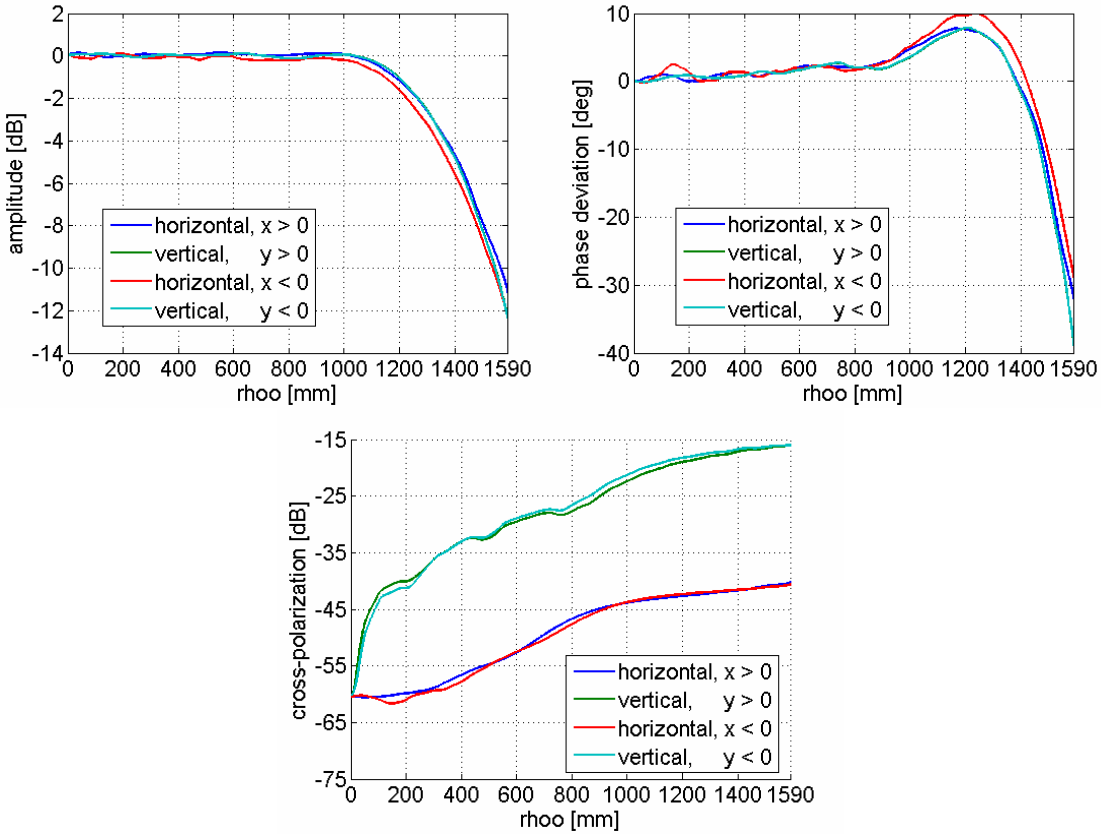

Figure 6.7. Simulated amplitude, phase deviation and cross-polarization of the 650 GHz DRFS at horizontal polarization.

The asymmetry of the feed horn radiation pattern is not taken into account in the synthesis and the input field is averaged in the rotationally symmetric mapping as explained in Sections 4.3.5 and 5.3. This results into the so called mapping error. If the asymmetry of the simulated feed horn radiation pattern would be taken into the account at the vertical polarization, the mapping error at the horizontal polarization would be double instead of the same, but in a different direction. The rotational symmetry assumption in the synthesis method enables the use of the DRFS at both vertical and horizontal polarizations.

6.6 DRFS operation at 310 GHz

The simulations were done also at the vertical polarization at 310 GHz using simulated radiation pattern of the feed horn used in the 310 GHz DRFS. The beam width of the 310 GHz feed horn is about the same as the beam width of the 650 GHz feed horn, but the beam shape is slightly different. The main difference in the beam shape is about 2 dB higher edge illumination of the subreflector. The 650 GHz DRFS was designed mechanically so that both the 310 GHz horn and the 650 GHz horn can be used, i.e. so that the phase centre point of either horn can be positioned to the correct location, as explained in Section 5.5. The simulation results are presented in Figure 6.8.

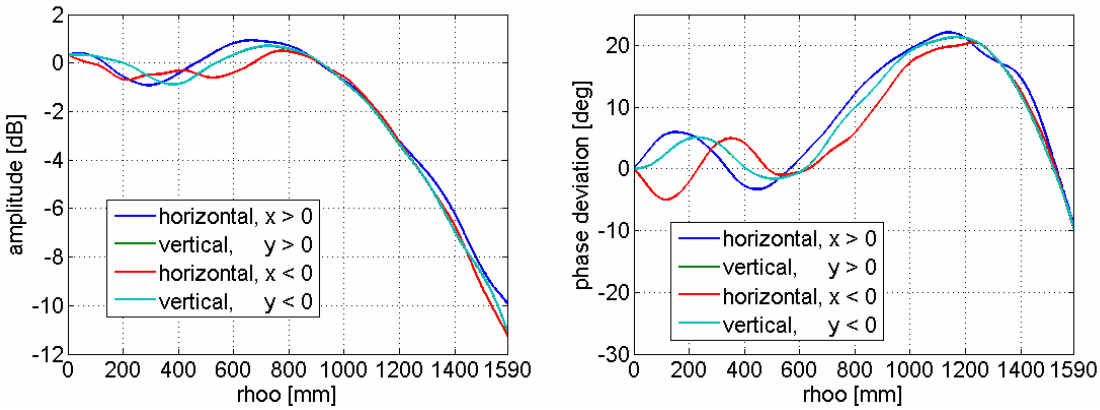

Figure 6.8 Simulated amplitude and phase deviation at 310 GHz.

The 310 GHz measurements may be used to verify that the DRFS has been manufactured accurately and how well the simulation results correspond to the measurements. These simulation results may be needed to verify the correct operation of the DRFS because the measurements at 650 GHz may be difficult to do accurately.

7 Discussion and future work

In this chapter the inaccuracies of the synthesis method are discussed. In addition, future work and possible improvements are discussed. The errors caused by the synthesis method can be divided into the mapping errors and the reflector surface synthesis errors. The errors in DRFS beam can be divided into the errors in the shape of the beam and to the ripple.

The rotationally symmetric mapping cause the mapping error, i.e., the input field used in the synthesis method is rotationally symmetric instead of being slightly wider in horizontal direction and narrower in vertical direction, compared to the simulated feed horn radiation pattern. When the DRFS is used at the horizontal polarization, the feed horn is rotated 90° and then the mapping error is equal but the input field used in the synthesis is narrower in the horizontal direction and wider in the vertical direction, compared to the simulated feed horn radiation pattern. If the asymmetry of the simulated feed horn radiation pattern would be taken in to account in the mapping at the vertical polarization, the mapping error at horizontal polarization would be double instead of equal. Therefore, because the input field is averaged in the rotationally symmetric mapping, the DRFS can be used at both vertical and horizontal polarizations.

The reflector synthesis errors are caused by the fact that the tangential planes used in the synthesis of the reflector surfaces are not the tangential planes of the final synthesized reflector surfaces. The tangential planes in the synthesis are calculated from the anterior rays, i.e., the previous ray ring, using the Snell's law. The tangential plane at the anterior point is the tangential plane that the reflector surface should have at that point. The shape of the synthesized reflector surfaces are defined as the interception points of the rays. If the shaping is very strong, i.e., the desired output field changes rapidly compared to the input field, the synthesis error is larger. This can be seen as the shoulder shape in the amplitude, as explained in Section 5.4. The synthesis error is also a function of the x-coordinate, because of the offset structure, i.e., because the incident angles of the rays on the tangential planes are different. This makes the output beam different in horizontal and vertical cuts and makes the horizontal cut asymmetric. In addition, the ray path length adjustment affects the synthesis error. The ray path length does not change rapidly,

therefore it does affect as much as the synthesis error that is caused by the change in the amplitudes.

The synthesis errors can be mostly compensated by optimizing the phase of the desired output field in the synthesis. The phase of the desired output field affects the desired ray path length, which affects the point on the main reflector, the ray from the subreflector to the main reflector, the tangential planes and therefore also the next points on both the subreflector and the main reflector.

In theory, the phase of the desired output field is the only frequency dependent part of the synthesis method as the relative electrical path length depends on the wavelength. In practice, also the effect of the synthesis errors, diffraction and manufacturing errors are frequency dependent. By optimizing the phase of the desired output field the synthesis errors have been compensated at 650 GHz.

The differences between the desired hologram illumination and the simulated results can be divided into the errors in the shape of the beam and to the ripple. The errors in the shape of the beam are mainly caused by the reflector synthesis errors, but also the mapping error has an effect. The ripples are mainly caused by the edge diffractions. The edge illuminations on the reflectors have been minimised.

In the design of a DRFS it is important to understand how everything affects everything. The parameters of the basic geometry are chosen mostly based on the requirements on the reflector size and the size of the whole DRFS. Also multiple reflections and direct radiation from the feed horn to the output aperture have to be considered. The input and output fields, i.e., the feed horn radiation pattern and the hologram illumination, are chosen based on the desired hologram illumination, so that the edge illuminations on the reflectors are minimised and the ratio of the input and output fields is optimized.

The assembly tolerances have been studied for the 310 GHz DRFS [Häkli 2004]. Misalignment and dislocation of the feed horn, the subreflector and the main reflector were studied with simulations. In general, mechanical tolerances are proportional to wavelength. The mechanical inaccuracies will affect the beam shape and the operation of the DRFS.

The numerical accuracy of the synthesis method has been studied by comparing synthesized non-shaped reflectors to ideal hyperboloid surfaces [Häkli 2004], [Häkli 2005a]. The number of rays needed for surface accuracy $\lambda/100$ is about 200×200 at 300 GHz and about 400×400 at 600 GHz [Häkli 2005a]. It is important to note that for the synthesized shaped surfaces the synthesis errors caused by the shaping are typically much larger than the errors caused by the finite number of rays. The number of rays used in the synthesis of the 650 GHz DRFS was mainly chosen to avoid problems with interpolations.

In the future the designed 650 GHz DRFS will be measured at 310 GHz and at 650 GHz. The use of a polarization grid will be studied to reduce the cross-polarization. Later, the designed 650 GHz DRFS will be used in a hologram-based CATR to measure a 1.5 metre reflector antenna at 650 GHz.

The possibility of using a different basic geometry than the dual hyperboloid geometry should be studied. The basic geometry can be optimized to achieve lower cross-polarization level in the hologram illumination. For example, a hyperboloid-ellipsoid structure could result into a more compact structure and lower cross-polarization level. Using an elliptical hologram illumination, instead of rotationally symmetric, could be also studied. The -1 dB area in the quiet-zone is narrower in the horizontal direction, when a rotationally symmetric illumination is used, because of the offset angle of the CATR as shown in Figure 2.2. Larger quiet-zone could be achieved with elliptical illumination. The synthesis method could be extended for elliptical fields by using elliptical ray grids. The optimal hologram illumination is still not known.

8 Conclusions

A 650 GHz dual reflector feed (DRFS) system has been designed. The DRFS was optimized to illuminate a 3.18 metre diameter hologram in a hologram-based compact antenna test range (CATR). The DRFS will be used in a hologram-based CATR to test a 1.5 metre antenna at 650 GHz.

The reflector surfaces of the DRFS were synthesized using a previously developed geometrical optics (GO) based numerical dual reflector synthesis method. The DRFS was optimized based on the simulations with GRASP8W that were done with physical optics (PO) and sometimes also physical theory of diffraction (PTD). Previously, a 310 GHz DRFS, designed with the same synthesis method, has been demonstrated for a hologram-based CATR. The designed 650 GHz DRFS has a wider beam and better beam quality.

The simulation results of the 650 GHz DRFS are clearly better than the minimum requirements defined in the beginning of the design process. The simulated -1 dB beam radius is about 1170 mm (74% of the hologram radius) and the hologram edge illumination is less than -10 dB. The amplitude ripple in the -1 dB beam area is at maximum 0.45 dB peak-to-peak (0.24 dB rms) and the maximum phase deviation is 5° peak-to-peak (0.8° rms). The -1 dB beam width of the DRFS corresponds to a 1.96 metre diameter quiet-zone (QZ). The cross-polarization of the DRFS is relatively high, in the -1 dB beam area at maximum -18 dB and near the hologram edges up to -15 dB in the vertical cut. To reduce the cross-polarization level, the possibility of using a polarization grid in front of the DRFS will be studied later. The dimensions of the reflectors are 146 mm × 109 mm × 7.0 mm, for the concave subreflector, and 203 mm × 160 mm × 4.4 mm, for the convex main reflector. The size of the whole DRFS is about 400 mm × 210 mm × 270 mm.

It was found that for minimal ripple the edge illuminations on the reflectors have to be minimised. For a desired beam width of the hologram illumination, it is most important to optimize the feed horn beam width and the shape of the desired output field amplitude. The output field amplitude and phase can be modified by optimizing the desired output field phase.

References

[Ala-Laurinaho 1997] J. Ala-Laurinaho, T. Hirvonen, J. Tuovinen, and A. V. Räisänen, Numerical modeling of a nonuniform grating with FDTD, *Microwave and Optical Technology Letters*, Vol. 15, No 3, pp. 134-139, June 1997.

[Ala-Laurinaho 2006] J. Ala-Laurinaho, J. Häkli, A. Karttunen, T. Koskinen, A. Lönnqvist, J. Mallat, M. Vaaja, V. Viikari, A. V. Räisänen, and J. Lemanczyk, Hologram-based CATR measurement of a 1.5 m antenna at 650 GHz: Progress report, *Proceedings of 4th ESA Workshop on Millimetre-Wave Technology and Applications 8th Topical Symposium on Millimeter Waves – TSMMW2006 7th Millimeter-Wave International Symposium – MINT-MIS2006*, 15-17 February 2006, Espoo, Finland, pp. 437-442.

[Albertsen 1985] N. Albertsen, K. Pontoppidan, and S. Sorensen, Shaping of dual reflector antennas for improvement of scan performance, *Antennas and Propagation Society International Symposium, 1985*, Vol. 23, Jun 1985, pp. 357-360.

[Bergmann 1988] J. Bergman, R. C. Brown, P. J. B. Clarricoats, and H, Zhou, Synthesis of shaped-beam reflector antenna patterns, *IEE Proceedings*, Vol. 135, Pt. H, No.1, pp. 48-53. Feb. 1988.

[Bjøntegaard 1983] G. Bjøntegaard and T. Pettersen, An offset dual-reflector antenna shaped from near-field measurements, *IEEE Transactions on Antennas and Propagation*, Vol. 31, No. 6, pp. 973-977, Nov. 1983.

[Collin 1985] R. E. Collin, *Antennas and Radiowave Propagation*, McGraw-Hill Book Company, United States of America, 1985, 508 p.

[Descardeci 1997] J. R. Descardeci and C. G. Parini, Trireflector compact antenna test range, *IEE Proceedings - Microwaves, Antennas and Propagation*, Vol. 144, No. 5, pp. 305-310, Oct. 1997.

[Duan 1995] D.-W. Duan and Y. Rahmat-Samii, A generalized diffraction synthesis technique for high performance reflector antennas, *IEEE Transactions on Antennas and Propagation*, Vol. 43, No. 1, pp. 27-40, Jan. 1995.

[ESA] Research and Scientific Support Department, European Space Agency, Available: http://www.rssd.esa.int/SA/PLANCK/images/pictures/phaseb/Alcatel/Alcatel_prop_nobg.jpg

[Galindo 1964] V. Galindo, Design of a dual reflector antennas with arbitrary phase and amplitude distribution, *IEEE Transactions on Antennas and Propagation*, Vol. 12, No. 4, pp. 403-408, July 1964.

[Galindo-Israel 1987] V. Galindo-Israel, W. A. Imbriale, and R. Mittra, On the theory of the synthesis of single and dual offset shaped reflector antennas, *IEEE Transactions on Antennas and Propagation*, Vol. 35, No. 8, pp. 887-896, Aug. 1987.

[Habersack 1991] J. Habersack, H.-J. Steiner, and E. Dudok, Millimetre wave application up to 204 GHz of the compensated compact range, *IEE Colloquium on Antenna Measurements using the Compact Antenna Test Range*, 25 Jan 1991, pp. 3/1-3/7.

[Hay 1999] S. G. Hay, Dual-shaped-reflector directivity pattern synthesis using the successive projections method, *IEE Proceedings - Microwaves, Antennas and Propagation*, Vol. 146, No. 2, pp. 119-124, Apr. 1999.

[Hirvonen 1997] T. Hirvonen, J. Ala-Laurinaho, J. Tuovinen, and A. V. Räisänen, A compact antenna test range based on a hologram, *IEEE Transactions on Antennas and Propagation*, Vol. 45, No. 8, pp. 1270-1276, Aug. 1997.

[Hoerner 1978] S. von Hoerner, Minimum-noise maximum-gain telescopes and relaxation method for shaped asymmetric surfaces, *IEEE Transactions on Antennas and Propagation*, Vol. AP-26, No. 3, pp. 464-471, May 1978.

[Häkli 2004] J. Häkli, *Design of a dual reflector feed system for a hologram compact antenna test range*, Licentiate thesis, Helsinki University of Technology, 2004, 108 p.

[Häkli 2005a] J. Häkli, J. Ala-Laurinaho, and A. V. Räisänen, Numerical Synthesis Method for Designing a Shaped Dual Reflector Feed System, *IEE Proceedings – Microwaves, Antennas and Propagation*, Vol. 152, No. 5, pp. 311-318, Oct. 2005.

[Häkli 2005b] J. Häkli, T. Koskinen, A. Lönnqvist, J. Säily, V. Viikari, J. Mallat, J. Ala-Laurinaho, J. Tuovinen, and A. V. Räisänen, Testing of a 1.5-m reflector antenna at 322 GHz in a CATR based on a hologram, *IEEE Transactions on Antennas and Propagation*, Vol. 53, No. 10, pp. 3142-3150, Oct. 2005.

[Häkli 2005c] J. Häkli, T. Koskinen, J. Ala-Laurinaho, and A. V. Räisänen, Dual reflector feed system for hologram-based compact antenna test range, *IEEE Transactions on Antennas and Propagation*, Vol. 53, No. 12, pp. 3940-3948, Dec. 2005.

[Jensen 2003] F. Jensen, *Reference Manual for GRASP8*, Ticra engineering consultants, 2003.

[Kildal 1990] P. S. Kildal, Synthesis of multireflector antennas by kinematic and dynamic ray tracing, *IEEE Transactions on Antennas and Propagation*, Vol. 38, No. 10, pp. 1587-1599, Oct. 1990.

[Koskinen 2005] T. Koskinen, J. Ala-Laurinaho, J. Säily, A. Lönnqvist, J. Häkli, J. Mallat, J. Tuovinen, and A. V. Räisänen, Experimental study on a hologram-based compact antenna test range at 650 GHz, *IEEE Transactions on Microwave Theory and Techniques*, Vol. 53, No. 9, pp. 2999-3006, Sep. 2005.

[Lehto 2001] A. Lehto and A. Räisänen, *Mikroaaltomittaustekniikka*, Otatieto, No. 875, Helsinki 2001, 215 p.

[Lindell 1997] I. Lindell and K. Nikoskinen, *Antenniteoria*, Otatieto, No. 848, Helsinki 1997. 347 p.

[Luh 1997] H. H. S. Luh, Antenna geometries for shaped dual reflector antennas, *Digest of IEEE Antennas and Propagation Society International Symposium*, 1997, pp. 1398-1401.

[Lönnqvist 2003] A. Lönnqvist, J. Mallat, and A. V. Räisänen, A phase hologram based compact RCS range for scale models, *Proceedings of the 25th Annual Meeting & Symposium of the Antenna Measurement Techniques Association (AMTA)*, October 19-20, 2003, Irvine, CA, pp. 118-123.

[Lönnqvist 2005] A. Lönnqvist, T. Koskinen, J. Häkli, J. Säily, J. Ala-Laurinaho, J. Mallat, V. Viikari, J. Tuovinen, and A. V. Räisänen, Hologram-based compact range for submillimeter-wave antenna testing, *IEEE Transactions on Antennas and Propagation*, Vol. 53, No. 10, pp. 3151-3159, Oct. 2005.

[Mizugutch 1976] Y. Mizugutch, M. Akagawa, and H. Yokoi, Offset dual reflector antenna, *Antennas and Propagation Society International Symposium, 1976*, Vol. 14, Oct 1976, pp. 2-5.

[Noponen 2006] E. Noponen, J. Häkli, T. Koskinen, A. Lönnqvist, V. Viikari, J. Ala-Laurinaho, J. Mallat, and A. V. Räisänen, Synthesis of reflector-type phase hologram for compact antenna test range at 310 GHz, *Proceedings of 4th ESA Workshop on Millimetre-Wave Technology and Applications 8th Topical Symposium on Millimeter Waves – TSMMW2006 7th Millimeter-Wave International Symposium – MINT-MIS2006*, 15-17 February 2006, Espoo, Finland, pp. 391-396.

[Pontoppidan 2003] K. Pontoppidan, *Technical Description of GRASP8*, Ticra engineering consultants, 2003, 376 p.

[Rubiños-López 1997] J. O. Rubiños-Lòpez and A. García-Pino, A ray-by-ray algorithm for shaping dual-offset reflector antennas, *Microwave and Optical Technology Letters*, Vol. 15, No. 1, pp. 20-26, May 1997.

[Räisänen 2003a] A. V. Räisänen, A. Lönnqvist, J. Mallat, E. Noponen, J. Ala-Laurinaho, J. Säily, T. Koskinen, and J. Häkli, A compact RCS-range based on a phase hologram for scale model measurements at sub-mm-wavelengths, *MWP 2003 Proceedings. International Topical Meeting on Microwave Photonics, 2003*, 10-12 Sept. 2003, Budapest, Hungary, pp. 55-56.

[Räisänen 2003b] A. V. Räisänen and A. Lehto, *Radio Engineering for Wireless Communication and Sensor Applications*, Artech House, Boston 2003, 396 p.

[Ticra] Ticra engineering consultants, Available: http://www.ticra.com/

[Viikari 2005] V. Viikari, J. Häkli, J. Ala-Laurinaho, J. Mallat, and A. V. Räisänen, A feed scanning based APC technique for compact antenna test ranges, *IEEE Transactions on Antennas and Propagation*, Vol. 53, No. 10, pp. 3160-3165, Oct. 2005.

[Westcott 1981] B. S. Westcott, F. A. Stevens, and F. Brickell, GO synthesis of offset dual reflectors, *IEE Proceedings*, Vol. 128, Pt. H, No. 1, pp. 11-19, 1981.

[Westcott 1993] B. S. Westcott, A. A. Zaporozhets, and A. D. Searle, Smooth aperture distribution synthesis for shaped beam reflector antennas, *Electronic Letters*, Vol. 14, No. 14, pp. 1275-1276, July 1993.